

Weak Faults at Megathrust Plate Boundary Respond to Tidal Stress

Takashi Tonegawa (✉ tonegawa@jamstec.go.jp)

Japan Agency for Marine-Earth Science and Technology <https://orcid.org/0000-0002-3173-4934>

Toshinori Kimura

Japan Agency for Marine-Earth Science and Technology: Kaiyo Kenkyu Kaihatsu Kiko

Kazuya Shiraishi

Japan Agency for Marine-Earth Science and Technology: Kaiyo Kenkyu Kaihatsu Kiko

Suguru Yabe

National Institute of Advanced Industrial Science and Technology Geological Survey of Japan: Sangyo Gijutsu Sogo Kenkyujo Chishitsu Chosa Sogo Center

Yoshio Fukao

Japan Agency for Marine-Earth Science and Technology: Kaiyo Kenkyu Kaihatsu Kiko

Eiichiro Araki

Japan Agency for Marine-Earth Science and Technology: Kaiyo Kenkyu Kaihatsu Kiko

Masataka Kinoshita

The University of Tokyo: Tokyo Daigaku

Toshinori Sanada

Japan Agency for Marine-Earth Science and Technology: Kaiyo Kenkyu Kaihatsu Kiko

Seiichi Miura

Japan Agency for Marine-Earth Science and Technology: Kaiyo Kenkyu Kaihatsu Kiko

Yasuyuki Nakamura

Japan Agency for Marine-Earth Science and Technology: Kaiyo Kenkyu Kaihatsu Kiko

Shuichi Kodaira

Japan Agency for Marine-Earth Science and Technology: Kaiyo Kenkyu Kaihatsu Kiko

Full paper

Keywords: Ambient noise, Seafloor observation, Ps reflection, Ship noise, Tidal response, Megasplay fault

Posted Date: November 18th, 2020

DOI: <https://doi.org/10.21203/rs.3.rs-109735/v1>

License: © ⓘ This work is licensed under a Creative Commons Attribution 4.0 International License.

[Read Full License](#)

Version of Record: A version of this preprint was published at Earth, Planets and Space on April 15th, 2021. See the published version at <https://doi.org/10.1186/s40623-021-01414-3>.

1 **Title page:**

2 **Title: Weak faults at megathrust plate boundary respond to tidal stress**

3 **for *Earth, Planets and Space* Version 20201109**

4 Author #1: Takashi Tonegawa, Japan Agency for Marine-Earth Science and Technology

5 (JAMSTEC), 2-15, Natsushima-cho, Yokosuka, 237-0061, Japan,

6 tonegawa@jamstec.go.jp

7 Author #2: Toshinori Kimura, Japan Agency for Marine-Earth Science and Technology

8 (JAMSTEC), 2-15, Natsushima-cho, Yokosuka, 237-0061, Japan,

9 kimurat@jamstec.go.jp

10 Author #3: Kazuya Shiraishi, Japan Agency for Marine-Earth Science and Technology

11 (JAMSTEC), 2-15, Natsushima-cho, Yokosuka, 237-0061, Japan,

12 kshiraishi@jamstec.go.jp

13 Author #4: Suguru Yabe, National Institute of Advanced Industrial Science and

14 Technology, 1-1-1, Umezono, Tsukuba, Ibaraki, 305-8560, Japan, s.yabe@aist.go.jp

15 Author #5: Yoshio Fukao, Japan Agency for Marine-Earth Science and Technology

16 (JAMSTEC), 2-15, Natsushima-cho, Yokosuka, 237-0061, Japan,

17 fukao@jamstec.go.jp

18 Author #6: Eiichiro Araki, Japan Agency for Marine-Earth Science and Technology

19 (JAMSTEC), 2-15, Natsushima-cho, Yokosuka, 237-0061, Japan,

20 araki@jamstec.go.jp

21 Author #7: Masataka Kinoshita, The University of Tokyo, 1-1-1, Yayoi, Bunkyo, 113-

22 0032, Japan, masa@eri.u-tokyo.ac.jp

23 Author #8: Sanada Yoshinori, Japan Agency for Marine-Earth Science and Technology

24 (JAMSTEC), 2-15, Natsushima-cho, Yokosuka, 237-0061, Japan,

25 sanada@jamstec.go.jp

26 Author #9: Seiichi Miura, Japan Agency for Marine-Earth Science and Technology

27 (JAMSTEC), 2-15, Natsushima-cho, Yokosuka, 237-0061, Japan,

28 miuras@jamstec.go.jp

29 Author #10: Yasuyuki Nakamura, Japan Agency for Marine-Earth Science and

30 Technology (JAMSTEC), 2-15, Natsushima-cho, Yokosuka, 237-0061, Japan,

31 yasu@jamstec.go.jp

32 Author #11: Shuichi Kodaira, Japan Agency for Marine-Earth Science and Technology

33 (JAMSTEC), 2-15, Natsushima-cho, Yokosuka, 237-0061, Japan,

34 kodaira@jamstec.go.jp

35

36 **Indicate the corresponding author**

37 **T. Tonegawa (tonegawa@jamstec.go.jp)**

38

39

40 **Abstract**

41 **Lateral spatial variations of weak portions at the plate boundary in subduction**
42 **zones have been estimated primarily by the distribution of slow earthquakes**
43 **mainly occurring around seismogenic zones. However, the detailed depth profile of**
44 **weak faults remains elusive. Here, we deployed 6 ocean bottom seismometers in**
45 **the Nankai subduction zone, Japan, to observe reflections originated from drilling**
46 **vessel *Chikyu* ship noise (hydroacoustic *P* wave) that was persistently radiated**
47 **from a fixed position at the sea surface, and retrieved *P*-to-*s* (*Ps*) reflections from**
48 **multiple dipping faults near the plate boundary. The *Ps* amplitudes were stacked**
49 **and compared according to the degrees of tidal stresses, and they were large at**
50 **high tide (compression). A migration technique shows that the locations where**
51 **velocity contrasts fluctuate were estimated at both the megasplay fault and**
52 **another fault between the megasplay fault and the top of the oceanic crust. This**
53 **indicates that the physical properties of those faults are changed by tidal stress.**
54 **The physical-property changes are attributed to fluid connections and isolations**
55 **within the faults due to tidal stress fluctuations, inducing the variation of seismic**

56 **anisotropy. Such a variation was confirmed by a three-dimensional numerical**
57 **simulation for wave propagation with anisotropic medium. Our observation**
58 **suggests that multiple weak faults are present around the plate boundary, and the**
59 **obtained changes of fault physical properties may have implications for our**
60 **understanding of tidal triggering of earthquakes.**

61

62 **Keywords**

63 Ambient noise, Seafloor observation, Ps reflection, Ship noise, Tidal response,

64 Megasplay fault

65

66 **Main Text**

67 **Introduction**

68 Tidal stresses result from the deformation of the Earth and ocean loading due
69 to the gravitational pull of the Sun and Moon, and these can trigger ordinary (Cochran
70 et al. 2004; Tanaka et al. 2006; Ide et al. 2016) and slow earthquakes (Rubinstein et al.
71 2008; Nakata et al. 2008; Lambert et al. 2009; Ide 2010) by stress fluctuations on plate

72 boundaries in subduction zones. The tidal sensitivity of slow earthquakes is affected by
73 the fluids within faults (Hawthorne and Rubin 2010; Houston 2015; Yabe et al. 2015;
74 Nakamura and Kakazu 2017). Under wetter conditions, the physical properties of the
75 plate boundary and thereby its frictional properties are presumably affected by external
76 periodic forces. However, there has been little observation on the tidal response of
77 plate-boundary properties because it requires continuous natural or artificial seismic
78 sources as well as persistent retrieval of seismic waves sampling the boundary. The
79 discovery of such phenomena could allow for the identification of mechanically weak
80 faults that are closely linked to rupture propagations of megathrust earthquakes and
81 tsunami generation, and this could be the key to understanding tidal triggering of
82 earthquakes.

83 A scientific drilling project was carried out between October 2018 and March
84 2019 by the International Ocean Discovery Program (IODP) with the drilling vessel
85 D/V *Chikyu* (hereafter *Chikyu*) (IODP expedition 358) (Fig. 1) at the C0002 site located
86 off the Kii Peninsula in the Nankai subduction zone, Japan, beneath which recurring
87 slow slip events have occurred around the plate boundary (Araki et al. 2017). Because

88 the *Chikyu* has a potential to excite incessant seismic sources during the project, we
89 installed 6 ocean bottom seismometers (OBSs) at distances ranging between 100–800 m
90 from the drilling site in the period from November 2018 to May 2019 to retrieve
91 seismic reflections beneath the seafloor originated from the *Chikyu*.

92 Seismic interferometry is capable of detecting waves propagating between
93 two receivers by cross-correlating the ambient noise recorded at both the receivers
94 (Shapiro 2005; Brenguier et al. 2007). Applying this technique to continuous seismic
95 records observed at a near-vertical array of OBS04 and a borehole sensor (Kopf et al.
96 2011; Kopf et al. 2016) (Fig. 1b), we found that the downgoing P waves generated by
97 the *Chikyu* ship noise were dominant during the non-drilling period, while upgoing S
98 waves from the drill-bit torque at depth could be observed in the drilling period (See
99 details in Materials and Methods section): *Chikyu* produces hydroacoustic P waves in
100 the sea water by, e.g., internal instrumental and external thruster noises, from the fixed
101 drilling position at the sea surface, and they are converted to downgoing P waves at the
102 seafloor. Therefore, we examined the *Chikyu* ship-noise records acquired by the 6 OBSs
103 during the non-drilling periods of the project, in order to persistently retrieve the

104 seismic waves reflected from downgoing P waves at the deep structure around the plate
105 boundary.

106 In the Materials and Methods section, we confirm the wavefield near the
107 seafloor during non-drilling period with seafloor and borehole sensors, correct the
108 amplitudes of the 6 OBSs with site amplifications, and extract reflections through a
109 deconvolution technique from both airgun shot experiments conducted by two vessels
110 and *Chikyu* ship noise. In the Results section, we compare the amplitude variations of
111 reflections in the deconvolved waveforms using the calculated tidal stresses, and image
112 the locations, where the effects of tidal stress can be observed, through a migration
113 technique. We finally discuss a possible model that explains reflection amplitudes
114 induced by tidal stresses.

115

116 **Materials and Methods**

117 **Ambient noise wavefield during the drilling period**

118 Six ocean-bottom seismometers (OBSs) were installed at a range of distances
119 between 100 m and 800 m from C0002. Four OBSs were placed at 100, 100, 200 and

120 250 m by the remotely operated vehicle (ROV) installed on D/V *Chikyu* and the two
121 remaining OBSs were dropped in free-fall from R/V *Yokosuka* at 700 and 800 m from
122 the drilling site; their location errors are ~2 m and 10–20 m, respectively.

123 To investigate the ambient noise wavefield during the drilling project, we
124 calculated the cross-correlation function (CCF) of continuous records observed by
125 OBS04 and a borehole sensor that is deployed at a depth of 900 m beneath the seafloor
126 (Figs. 1**b** and 2**a**) (Kopf et al. 2011; Kopf et al. 2016). The OBS contains a 4.5 Hz short-
127 period sensor with three components. The length of time window was 80 s. Spectral
128 whitening was performed during the calculation of the CCF (Brenquier et al. 2007).
129 Because we have the rotation speed information of the drill-bit (RPM: rotation per
130 minute) in the drilling vessel (D/V) *Chikyu* (hereafter *Chikyu*) (Fig. 2**b**), the CCFs
131 averaged over a one-hour period using ambient noise records of the vertical component
132 (ZZ) between the two sensors were calculated for two conditions: RPMs of 0 (non-
133 drilling period) and 32 (drilling period). This processing was also performed using the
134 transverse component (TT), in which the transverse direction at the two sensors is
135 perpendicular to the directions from the *Chikyu* to the two sensors.

136 Figure 2d shows four CCFs (ZZ and RPM = 0, ZZ and RPM = 32, TT and
137 RPM = 0, and TT and RPM = 32). Because the reference site is OBS04 (seafloor) for
138 the CCF calculation, peaks with large amplitudes at the positive/negative lag time in the
139 CCFs represent the downgoing/upgoing wave. The ZZ-CCF for RPM = 0 shows the
140 downgoing P wave at a lag time of 0.5 s, and the TT- and ZZ-CCFs for RPM = 32 show
141 the upgoing S wave at a lag time of 1.8 s. This means that the upgoing S wave and
142 downgoing P wave are dominant in the ambient noise wavefield during the drilling and
143 non-drilling period, respectively.

144

145 **Correction on the amplification of seafloor records**

146 Seismic waves observed at the seafloor are amplified by soft materials in the
147 marine sediments at shallow depths (Yabe et al. 2015). The amplified amplitudes at the
148 OBS are corrected by zero or weak amplification of those observed at the borehole
149 sensor. We used four deep earthquakes associated with the Pacific Plate subducting
150 beneath the Japanese Island (Table 1). The epicenters of these events are located within
151 200 km from the drilling site, which ensures near-vertical incidence of *P* wave into the

152 OBSs. W_{ij} is the root mean squared amplitude (RMS) of the vertical component for the
153 i -th event and the j -th station, and is given by

$$154 \quad W_{ij} = \frac{\sqrt{w_{ij}^2(t)}}{\sqrt{w_{i0}^2(t)}}, \quad (1)$$

155 where w_{ij} and w_{i0} are the vertical components at an OBS and borehole sensor,
156 respectively, for a time window from -1 to 9 s from the P arrival time. The RMS of the
157 horizontal component, H_{ij} , is defined as

$$158 \quad H_{ij} = \frac{\sqrt{u_{ij}^2(t)+v_{ij}^2(t)}}{\sqrt{u_{i0}^2(t)+v_{i0}^2(t)}}, \quad (2)$$

159 where u_{ij} , v_{ij} and u_{i0} , v_{i0} are the horizontal components at an OBS and borehole sensor,
160 respectively. Using these at a frequency band of 5 – 15 Hz, the site amplification factors
161 for the vertical and horizontal components at the j -th station can be written as

$$162 \quad W_j = \frac{\sum_{i=1}^4 W_{ij}}{4}, \quad H_j = \frac{\sum_{i=1}^4 H_{ij}}{4}. \quad (3)$$

163 The estimated values for each of these variables are summarized in Table 2. The
164 estimated values for different events were stable, which led to small errors. Although
165 the amplification factors in the horizontal component are larger than those in the vertical
166 component, such large values were also obtained previously in this region (Kubo et al.

167 2018; Yabe et al. 2019). Moreover, based on this correction, in the Discussion section,
168 we do not incorporate sediment layers in numerical simulations when comparing the
169 observed and calculated amplitudes.

170

171 **Ps reflections from inline airgun shots within ± 10 km**

172 Research Vessel (R/V) *Kaimei* (hereafter *Kaimei*) performed successive
173 airgun shots along the NNW–SSE trending line within ± 10 km from the drilling site
174 (Fig. 3). Figure 3b shows the three-component seismic records, where two *P*-to-*s* (*Ps*)
175 reflected waves can clearly be seen in the two horizontal components. When a gently
176 dipping interface, i.e., a megasplay fault, is present beneath the seafloor, a reflected *P*
177 wave emerges at a nearly constant two-way travel time within an offset of 10 km
178 (Nakanishi et al. 2008): the megasplay fault is a major out-of-sequence thrust fault
179 splayed off the plate interface. When the offset is small, a *Ps* wave can also be observed
180 in the same way. Based on *Ps* – *P* times of 6.1 and 7.6 s, a *V_p* model (Shiraishi et al.
181 2019), and an empirical relation between *V_p* and *V_s* (Brocher 2005), two *Ps* waves are
182 reflected from the megasplay fault at a depth of 7 km and the top of the oceanic crust at

183 a depth of 9 km. For example, using a V_p of 3.70 km s⁻¹ between the megasplay fault
184 and the top of the oceanic crust (Shiraishi et al. 2019), we obtain a V_s of 2.02 km s⁻¹
185 from the empirical relation (Brocher 2005). Using the differential travel time of 1.5 s,
186 we obtained a thickness of 1.96 km between the two reflections.

187

188 **Ps reflections from airgun shot and ship noise by *Chikyu***

189 Although the inline-shot records from *Kaimei* are useful for detecting Ps
190 signals, fixed-point airgun shots from *Chikyu* are more effective to compare with Ps
191 signals retrieved from *Chikyu* ship noise, because ship noise and airgun shots are
192 generated from almost exactly the same location, whereas *Kaimei* was at least 400 m
193 away from *Chikyu*.

194 To retrieve Ps signals from airgun shot and ship noise, we applied a
195 deconvolution technique in the frequency domain (e.g., Langston 1979; Ammon 1991)
196 to the three-component records with a bandpass filter of 9–15 Hz: the horizontal
197 component is divided by the vertical component in the frequency domain. Because we
198 divided the deconvolved waveform by the maximum amplitude of the auto correlation

199 of vertical component (Ammon 1991), the absolute P_s amplitudes are preserved
200 irrespective of different OBSs and temporally-varying strengths of ship noise. Prior to
201 the deconvolution, waveform amplitudes in the vertical and horizontal components were
202 divided by the site amplification factors in Table 2. The time windows for airgun and
203 ship noise (ambient noise) records were 20 s from the shot origin time and 80 s,
204 respectively. For ship noise, hourly and daily waveforms in the radial and transverse
205 components were obtained by stacking 80 s-deconvolved waveforms. Here, we only
206 used 1-hour waveforms when the stacked number of the 80 s-deconvolved waveforms
207 with $RPM = 0$ was > 40 among 45 segments ($\times 80 \text{ s} = 1 \text{ hour}$). This processing allows
208 us to use the continuous 1-hour records in which non-drilling periods are dominant.

209 In Figs. 4 and S1, the deconvolved waveforms from 20 airgun shots were
210 aligned at each OBS, while the daily waveforms from ambient noise on Julian days 1–
211 120 of 2019 were aligned, in which *Chikyu* was located onsite on Julian days 1–58 and
212 was away from the site after Julian day 59: this indicates that none of the signals after
213 Julian day 59 were caused by ship noise. In these figures, we focused on lag times of 4–
214 9 s by referring to P_s – P times of 6.1 s and 7.6 s at the megasplay fault and the top of the

215 oceanic crust. Non-drilling periods (RPM = 0) were relatively secured during days 1–58
216 in 2019 compared with the project period in 2018 (Fig. 2b), and the location of the
217 *Chikyu* was ranged within 10 m during the study period (Fig. 2c). Moreover, in order to
218 evaluate the similarity of the deconvolved waveforms, we estimated cross-correlation
219 coefficients (CCs) between the deconvolved waveforms using airgun shot and ship
220 noise records, with a time window of 0.1 s and a time shift of 0.05 s (Figs. 4 and S1).

221 Coherent signals between the two sources emerged at lag times of 5, 6, and
222 7.8 s in the radial-deconvolved waveforms (RDWs) at OBS03 (Fig. 4a), but signals
223 were clearer in the transverse component and could be observed at all OBSs (Figs. 4b
224 and S1). Here, the RDWs contain multiple peaks compared with the transverse-
225 deconvolved waveforms (TDWs) (Fig. 4). Those peaks may have originated from the
226 contamination of multiple reflections at shallow depth. In theory, the reflection
227 coefficient of *P*-to-*S* reflection from a horizontal boundary for a vertical incident angle
228 is zero. However, when the incident angle of the *P* wave and the boundary are slightly
229 deviated from the vertical direction and horizontal plane, the reflection and its multiple
230 reflections are possibly observed in the RDWs at smaller lag times and these are

231 deviated to other directions at larger lag times. Moreover, we estimated the CCs of the
232 RDWs and TDWs between airgun shots and ship noises, and coherent signals were
233 obtained with higher CCs in the TDWs (Fig. 4d). We therefore avoided the use of the
234 RDWs in the subsequent processing. Although all of the signals in the TDWs obtained
235 from the two sources were not completely matched, it is likely that the coherent signals
236 originated from the same structural boundaries beneath the seafloor, including the
237 megasplay fault, because peaks with high CC values could be observed in the TDWs
238 between the airgun shots and ship noises (Fig. S1).

239

240 **Stacking waveforms with tidal stress**

241 The tidal normal stress on the megasplay fault was calculated with a method
242 described in a previous study (Yabe et al. 2015). The geometry of the megasplay fault
243 was inferred with a strike = 270° and dip = 10° , which were set by referring to three-
244 dimensional reflections and velocity models in this region (Shiraishi et al. 2019). The
245 slip direction had a rake = 125° , which represents the thrust fault. The azimuth and
246 angle were defined as clockwise from north and downward from the horizontal plane.

247 Figure 5a shows the resulting normal stress on the megasplay fault, in which negative
248 values represent compression. We stacked 1-hour TDWs at each 5 days for the
249 following three ranges in normal stress at every OBS: high tide < -2.4 kPa, middle tide
250 between -2.4 kPa and 1.6 kPa, and low tide > 1.6 kPa (Fig. 5a). The envelope functions
251 were calculated by stacking 5-day TDWs during 10–50 Julian days when the number of
252 available TDWs were balanced among the three tide ranges (Figs. 6 and S2): during the
253 5 days, 120 hours (maximum) were divided by the three ranges of the tide, and we
254 counted the numbers of 1-hour TDWs in the three ranges (Fig. 5b). The above
255 thresholds for the three ranges of normal stress were determined so as to preserve the
256 number of 1-hour TDWs to at least 5 during every 5-day period and for each range.
257 Although the resulting counts on the 37th day were less due to the drilling periods (Fig.
258 2b) and the count for middle tide on the date was 5, those for high and low tides
259 exceeded 9. We therefore compared TDWs between high and low tides in this study.
260 The uncertainties of the envelope functions were the standard deviations obtained by
261 bootstrapping the 5-day TDWs for each tide range for 5,000 times with repetition (Figs.
262 6 and S2).

263 To investigate the stability of the amplitudes in the stacked TDWs, we plotted
264 5-day moving averages of the TDWs for the normal stress ranges of high and low tides
265 (Figs. 5c and d). Moreover, the delay time of each segment in the 5-day TDWs between
266 high and low tides was also estimated by cross-correlating them with a time window of
267 0.2 s and a time shift of 0.1 s (Figs. 5c and d). If some signals in the TDWs were
268 systematically delayed (or advanced) between high and low tides, the delay time should
269 have showed the coherent patterns at similar lag times.

270

271 **Migration P-to-s scattered amplitude and tidal-responded amplitude**

272 Using the three-dimensional V_p model (Shiraishi et al. 2019) and an empirical
273 relation between V_p and V_s (Brocher 2005), we calculated differential travel times
274 between direct P waves from *Chikyu* to an OBS and P -to- s (P_s) scattered waves in two-
275 dimensional transects. The amplitudes of the TDWs were plotted onto locations where
276 their lag times were matched with the differential times in the transects. Here, the
277 TDWs were stacked over 10–50 days at every OBS, and the amplitudes in the stacked
278 TDWs were assumed to have been due to P_s waves. The TDW amplitudes at lag times

279 of 5–9 s were used for imaging, where P_s waves reflected around the plate boundary
280 were expected. We only imaged below OBSs within a scattering angle of the P_s wave
281 less than 2° from the vertical axis, because the number of OBSs was small for imaging
282 the entire volume around the OBS array. The scattering angle was defined as the angle
283 between the incident P wave and the P_s wave at scattering points.

284 In addition to the raw amplitudes, we also created transects for displaying the
285 locations where amplitudes responded to tidal stress. To enhance the amplitude
286 variations in response to tidal forces, we calculated the amplified differential P_s
287 amplitudes (AD- P_s) between the envelope functions of the high-tide TDW, $S_H(t)$, and
288 low-tide TDW, $S_L(t)$,

$$289 \quad F(t) = \frac{R(t)}{|R(t)|} S_H(t) \cdot R(t)^2 \cdot C, \quad (4)$$

290 where

$$291 \quad R(t) = S_H(t) - S_L(t), \quad (5)$$

292 and C is an arbitrary constant which only makes the average amplitude of $F(t)$
293 comparable to that of $S_H(t)$. We chose C as 2.0×10^6 . $R(t)$ indicates the difference of P_s
294 amplitudes in the envelope functions of $S_H(t)$ and $S_L(t)$ (eq. (5)). The positive/negative

295 polarity in $R(t)$ represents the velocity contrast increase/decrease at seismic
296 discontinuities at high tide. When the large P_s amplitude in $S_H(t)$ and large P_s amplitude
297 difference in $R(t)$ occur of the same lag times, the peak amplitudes in the $S_H(t)$ were
298 amplified while preserving the polarities of $R(t)$. Thus, $F(t)$ shows P_s reflections from
299 seismic discontinuities with large impedance contrasts and large amplitude variations
300 between high and low tides. The examples of $S_H(t)$ and $F(t)$ at OBS03 and OBS06 are
301 displayed in Figs. 6**b** and S2**b**. Using these functions, we made ENE-WSW and NNW-
302 SSE trending transects (red lines in Fig. 1**b**) and projected them onto the reflection
303 images (Shiraishi et al. 2019) along nearby ENE-WSW and NNW-SSE trending lines
304 (yellow lines in Figs. 1**a** and **b**). Because AD- P_s at OBS01 was slightly large compared
305 with that at other OBSs and the amplitudes in the TDWs may have been unstable during
306 1–58 Julian days (Fig. S1**a**), we removed this station from imaging.

307

308 **Results**

309 **Tidal response of reflections**

310 To investigate whether the amplitudes and travel times of P_s waves respond

311 to tidal stress, we calculated the normal tidal stress, slip-parallel shear stress, and slip-
312 orthogonal shear stress on the megasplay fault (Yabe et al. 2015) by assuming its
313 geometry (Shiraishi et al. 2019) and thrust fault slip derived from the motion vector of
314 the underlying ocean plate (DeMets et al. 2010) (Fig. 5a). Figure 6 presents the
315 comparison of envelope TDWs using ship noise at high and low tide, mainly showing
316 larger peak amplitudes of *Ps* waves at high tide. This feature can be partially recognized
317 at OBS02 and OBS06 (Fig. S2), although some peaks show smaller amplitudes at high
318 tide. The stability of the larger amplitudes at high tide at OBS03 and OBS04 were also
319 confirmed by 5-day moving average of the TDWs (Fig. 5). In addition, the time-shift
320 estimation of waveform segments of the TDWs between high and low tide with a time
321 window of 0.2 s and a time increment of 0.1 s did not vary systematically (Figs. 5c and
322 **d**). These observations indicate that seismic velocity changes in the entire medium
323 associated with tidal stresses are minor, whereas velocity contrasts at the boundaries
324 within the accretionary prism fluctuated with tidal stress.

325

326 **Imaging of tidal responding boundaries**

327 Depth migrations of amplified differential P_s amplitudes (AD- P_s) between
328 high and low tide (eq. (4)) located where the velocity contrast fluctuates in the
329 accretionary prism. The P_s signals of the TDWs and the AD- P_s were strong at the
330 megasplay fault at a depth of 7 km, whereas those signals were weak at the top of the
331 oceanic crust at a depth of 9 km (Fig. 7). Here, for AD- P_s , a positive/negative amplitude
332 represents a correspondingly positive/negative enhancement of P_s amplitude at high
333 tide, respectively, and AD- P_s at three stations close to the line are plotted. Additionally,
334 the velocity contrast of a boundary at a depth of 8 km between the megasplay fault and
335 the top of the oceanic crust fluctuates with tidal stress. More of the clear features of the
336 two boundaries can be recognized in the NS-trending transect (Fig. 8).

337

338 **Discussion**

339 **Velocity reduction in isotropic case**

340 A seismic exploration survey revealed the negative amplitude of P waves
341 reflected at the megasplay fault (Park et al. 2002), which is indicative of a velocity
342 reduction within the fault. The larger positive amplitude observed at high tide in this

343 study indicates that the velocity reduction at the megasplay fault was further enhanced
344 by vertical compression caused by tidal stress.

345 In order to confirm the velocity reduction, we conducted a three-dimensional
346 finite-difference approach with rotated staggered grids and second-order calculation
347 accuracies in time and space (Saenger et al. 2000). The model space (x_1 - x_2 - x_3) was $8 \times$
348 $8 \times 6 \text{ km}^3$ and included four layers with a grid spacing of 0.01 km, and the x_3 -axis was
349 taken as vertically downward. The time step was 0.001 s. An absorbing boundary
350 condition was assigned to each side except for the top (Clayton and Engquist 1977). The
351 source location was set to $(x_1, x_2, x_3) = (4.0, 4.0, 0.0)$ at the model sea surface. A vertical
352 force with a Ricker wavelet at a center frequency of 7.59 Hz (maximum frequency of
353 10.96 Hz) was applied to the source location. The stations were assigned at the seafloor
354 locations (2 km depth) relative to the *Chikyu* in the observations (Fig. 9a). The V_p , V_s ,
355 and density of the homogeneous medium and fluid are 4.5 km s^{-1} , 2.25 km s^{-1} , and 2.5 g
356 cm^{-3} , and 1.5 km s^{-1} , 0.0 km s^{-1} , and 1.0 g cm^{-3} , respectively (Table 4), in which V_p is
357 roughly referred to an averaged V_p around the megasplay fault. In the isotropic case, a
358 V_s of 2.25 km s^{-1} at layer 3 was reduced by 1, 3, 7, and 13 % (Table 4). The fault

359 thickness was set to be 0.05 km (Rowe et al. 2013), in which V_p and V_p/V_s were
360 referenced to seismic exploration results (Shiraishi et al. 2019).

361 As a result, because the P_s amplitude difference is linear with respect to V_s
362 reduction, the observed amplitude difference, ~ 0.0002 in Fig. 6a, can be linked to a V_s
363 reduction of 1.5–3.3 % (Fig. 9b). In this calculation, P_s signals were not observed in the
364 transverse component at OBS05 and OBS06. The P_s amplitudes at these stations
365 obtained in our observation may have been produced by a focusing effect of P_s
366 amplitudes at a gently curved interface of the megasplay fault that was imaged by a 3D
367 seismic volume (Shiraishi et al. 2019), and so these were not used to estimate V_s
368 reductions. Because the obtained V_s reduction of 1.5–3.3 % is large and elastic property
369 perturbations linearly changed by the tidal stress are small, it is therefore necessary to
370 consider other mechanisms capable of significantly changing the seismic velocity of the
371 fault with small stress fluctuations and fluid concentrations.

372

373 **Fracture connection and isolation due to tidal stress**

374 A possible mechanism is fracture channeling with fluids in the fault by

375 external forces (e.g., (Hawthorne and Rubin 2010; Houston 2015)). Characteristic
376 fractures are formed around a through-going fault (Y shear) (Bartlett et al. 1981) within
377 the damage zone of a fault, with different direction groups including, e.g., Riedel (R)
378 shears and antithetic R' shears (Tchalenko and Ambraseys 1970). On land, these shear
379 zones are found in the latest Cretaceous Mugi mélange in southwestern Japan, and this
380 mélange is considered to be a fault rock along the plate boundary in the Nankai
381 subduction zone (Kimura et al. 2012). These fractures around the deep plate boundary
382 are potentially saturated with fluids, because the region between the fault and top of
383 oceanic crust is characterized by high pore pressures (Tsuji et al. 2014), and the land
384 mélange also shows evidence of fluid presence (Kimura et al. 2012). For a dip angle of
385 the megasplay fault of 10° in this region (Shiraishi et al. 2019), the R shears are oriented
386 close to horizontal (Fig. 10). When a small vertical-compressional stress is applied to R
387 shears, their shapes are slightly compressed in the vertical direction, and internal fluids
388 are expelled to Y shear and near-vertical R' shears following the fluid pressure gradient.
389 This results in fluid connections between shears, thereby enhancing seismic velocity
390 anisotropy within the megasplay fault. By this mechanism, negative AD-Ps would be

391 caused only when near-vertical R' shear expansion is prevalent and there is less
392 connectivity of Y shears in the fault-parallel direction.

393

394 **Numerical simulation in anisotropic case**

395 To qualitatively investigate large P_s amplitudes reflected at the megasplay
396 fault, we also conducted numerical simulations for models in which the degree of
397 anisotropy within the fault varied with the aspect ratio of cracks. Here, the assumptions
398 for an effective medium in the damage zone along the megasplay fault are that
399 highly/weakly connected fractures are described by inclusions of fault-oriented oblate
400 spheroidal cracks with a small/large aspect ratio, with a constant porosity of the bulk
401 medium at 0.07 by referring to the porosity < 0.07 of land outcrop samples that were
402 considered to be a fossil seismogenic megasplay fault rock (Tsuji et al. 2008).

403 The calculation of the effective elastic constants for a medium containing
404 fluid-filled fractures and their connections would be complicated. Instead, for the
405 purpose of this study, we assumed a simple model in which fluid filled oblate
406 spheroidal cracks, assuming Riedel shears, are horizontally developed within the

407 megasplay fault with a dip angle of 10° . When the cracks are partially connected by
408 fluid-filled fractures, such as Y and R' shears, due to an external force, individual
409 fracture lengths are extended along the fault-parallel direction. This would be expressed
410 by a slight decrease in the average aspect ratio of the cracks aligned to the fault-parallel
411 direction with minor porosity changes. The P wavelength used in this study is 300–500
412 m using a frequency of 9–15 Hz and a V_p of 4.5 km s^{-1} (Shiraishi et al. 2019), and the
413 fault thickness at the Nankai accretionary prism toe was estimated to be 47.5 m from
414 IODP Site C0007 (Rowe et al. 2013). Because the P wavelength is sufficiently large
415 compared to the fault thickness and therefore to the fracture sizes, the assumption that
416 fracture connections can be described by the changes in the average aspect ratio of
417 aligned cracks is acceptable.

418 We calculated effective elastic constants using differential effective medium
419 (DEM) theory for hexagonal symmetry, in which aligned oblate spheroidal cracks with
420 an aspect ratio are contained in a homogeneous medium of given porosity (0.07)
421 (Nishizawa 1982; Tonegawa et al. 2013). The effective elastic constants transformed
422 into those in which the axis was parallel to the normal direction of the megasplay fault

423 with a dip angle of 10° and strike = 270° by using the following equation (Nagaya et al.
 424 2008).

$$425 \quad c_{i'j'k'l'} = U_{ii'}U_{jj'}U_{kk'}U_{ll'}C_{ijkl}, \quad (6)$$

426 where the elastic constants C_{ijkl} ($i, j, k, l = 1, 2, 3$) are transformed into those $c_{i'j'k'l'}$
 427 defined in the $(x_1'-x_2'-x_3')$ coordinate system. C_{IJ} in Table 4 was converted into C_{ijkl} by
 428 using the relationships of $ij=11, 22, 33, 23, 13, 12$ when $i (=j) = 1, 2, 3, 4, 5, 6$ and

$$429 \quad C_{ijkl} = C_{jikl} = C_{ijlk} = C_{klij}. \quad (7)$$

430 The matrix elements $U_{ii'}$ can be written as

$$431 \quad U = \begin{pmatrix} \cos\xi\cos\lambda & \cos\xi\sin\lambda & -\sin\xi \\ -\sin\lambda & \cos\lambda & 0 \\ \sin\xi\cos\lambda & \sin\xi\sin\lambda & \cos\xi \end{pmatrix}, \quad (8)$$

432 where ξ and λ are the tilt angle of the symmetry axis measured from the x_3 -axis
 433 and the azimuth of the axis measured clockwise from north (x_1 -axis), respectively. We
 434 set $\xi = 10^\circ$ and $\lambda = 180^\circ$ in the numerical simulations. The converted physical
 435 parameters were inserted in layer 3 in Table 5. In the isotropic case (aspect ratio = 1.0),
 436 Vp and Vs in the layer were reduced from 4.50 to 4.25 km s^{-1} and from 2.25 to 2.15 km
 437 s^{-1} , respectively, because the porosity including fluids was set to 0.07. When the aspect
 438 ratio of cracks varied from 1.0, the fast and slow seismic velocities are slightly deviated

439 from those values. The aspect ratios are 0.2–1.0 with an increment of 0.2. The
440 calculated elastic constants are summarized in Table 4.

441 The results show that P_s amplitudes tend to increase as the aspect ratio of
442 cracks decreases following a nonlinear curve (Fig. 10), except for the result at OBS05
443 as well as the isotropic case. Thus, our results indicate that fault-parallel connections of
444 fractures produce large P_s amplitudes in our observation geometry, and that if fractures
445 are originally moderately connected (i.e. their aspect ratio is small), significant
446 amplitude variations can be induced by a small amount of additional connections
447 between fractures.

448 Moreover, we roughly estimated the preferred aspect ratio of cracks within
449 the megasplay fault in this region by using both our observation results and numerical
450 simulations. The observed P_s amplitude and its difference between high and low tides
451 were ~ 0.001 and ~ 0.0002 , respectively (Fig. 6). These values indicate that the aspect
452 ratio of cracks is close to 0.8–1.0, and that it varies within 0.6–1.0 between high and
453 low tides (Fig. 10). However, if the porosity within the megasplay fault was smaller
454 than 0.07, e.g., 0.05 in Fig. 11, the obtained P_s amplitudes became small, thus

455 indicating that the aspect ratio of cracks and its variation between high and low tides
456 would also be small. Because land outcrop samples within the fossil seismogenic
457 megasplay fault shows a dominant aspect ratio of cracks of 0.1–1.0 (Tsuji et al. 2008),
458 *Ps* amplitudes obtained in this study can be explained by the 0.1–1.0 aspect ratio of
459 cracks even if the porosity is slightly smaller than 0.05.

460 Moreover, using numerical simulations, we confirm whether the observed *Ps*
461 amplitudes are affected by (1) high velocity anomalies above the megasplay fault,
462 detected by a seismic exploration study (Shiraishi et al. 2019), and (2) small velocity
463 variations at shallow depths (Fig. 11). We examined the following two models: (1) a
464 higher velocity zone above the megasplay fault than that at shallow depths without
465 changing the velocity contrast at the megasplay fault, and (2) two layers above the
466 megasplay fault with velocity reductions of 2.5 % and 1.5 % and thicknesses of 0.05 km
467 and 0.03 km, respectively. The latter model assumes that other faults are present
468 between the seafloor and the megasplay fault, and their velocities are slightly changed
469 by tidal forces. As a result, the obtained *Ps* amplitudes were slightly changed in model
470 (1) from those in the original model but the characteristic in which *Ps* amplitudes

471 increase with decreasing the aspect ratio was not changed, while P_s amplitudes were
472 almost unchanged between models (1) and (2) (Fig. 11). This investigation indicates
473 that our results are not significantly affected by the velocity gradient and temporal
474 variations of velocity changes at shallow depth.

475

476 **Conclusion**

477 The physical properties of the plate boundary responding to tidal forces are
478 the important factor for understanding tidal triggering of earthquakes occurring at the
479 plate boundary. Such property changes are attributed to the presence and connection of
480 fluids within faults, and indicate the existence of mechanically weak interfaces.

481 Through the tidal response of reflection amplitudes, our study identified two such
482 parallel dipping faults around the plate boundary. Slow slip events in the shallow
483 Nankai subduction zone have been detected by pore pressure variations at the borehole
484 site (Araki et al. 2017) and also seafloor geodetic observations (Yokota and Ishikawa
485 2020), and they might have occurred at these multiple weak faults. Additionally, if the
486 physical properties of the weak portions within the megasplay fault have been

487 temporally varied with long-term fluid migration, and if the shear strength within the
488 fault had been very weak, such slow slip events could be possibly triggered by tidal
489 forces.

490

491 **Declarations**

492 **Ethics approval and consent to participate**

493 Not applicable

494 **Consent for publication**

495 Not applicable

496 **List of abbreviations**

497 OBS: ocean bottom seismometer, RDW: radial deconvolved waveform,

498 TDW: transverse deconvolved waveform, AD-Ps: amplified differential

499 Ps amplitude, ROV: remotely operated vehicle, D/V: drilling vessel,

500 R/V: research vessel, CCF: cross correlation function, ZZ: vertical

501 component correlation, TT: transverse component correlation, RPM:

502 rotation per minute, RMS: root mean square, V_p : *P*-wave velocity, V_s : *S*-

503 wave velocity, CC: cross correlation coefficient, *Ps*: *P*-to-*s*, R shear:

504 Riedel shear

505 **Availability of data and materials**

506 Seafloor seismometer data are available from JAMSTEC upon request.

507 The data that support the findings of this study are available from the

508 corresponding author upon reasonable request.

509 **Competing interests**

510 The authors declare no competing interests.

511 **Funding**

512 This study is supported by MEXT Grant-in-Aid for Scientific Research

513 on Innovative Areas (19H04632).

514 **Authors' contributions**

515 T.T processed the data, and drafted the manuscript. T.K. designed the

516 observation. K.S. prepared the data for reflection profiles and drilling

517 parameters of *Chikyu*. S.Y. calculated tidal stress. Y.F. and S.K.

518 contributed to the interpretation. T.T., T.K., K.S., E.A., M.K., Y.S., S.M.,

519 Y. N., and S. K. acquired the data underlying this study. All authors
520 contributed to the final manuscript.

521 **Acknowledgements**

522 We thank crews of D/V *Chikyu*, R/V *Kaimei*, and R/V *Yokosuka*, and
523 Takuya Onodera for supporting OBS deployment. We would also like to
524 thank the Associate Editor and three anonymous reviewers for their
525 constructive comments and useful suggestions. We used the time-series
526 data of drilling parameters during the IODP expedition 358. Bathymetry
527 was acquired by “Research Project for Compound Disaster Mitigation on
528 the Great Earthquakes and Tsunamis around the Nankai Trough Region”
529 of the Ministry of Education, Culture, Sports, Science and Technology
530 (MEXT) of Japan. We used the computer systems of the Earthquake and
531 Volcano Information Center of the Earthquake Research Institute, The
532 University of Tokyo.

533 **Authors' information**

534 *Japan Agency for Marine-Earth Science and Technology (JAMSTEC), 2-*

535 *15, Natsushima-cho, Yokosuka, 237-0061, Japan.*

536 T.T, T.K, K.S, Y.F, E.A, Y.S, S.M, Y.N, S.K

537 *National Institute of Advanced Industrial Science and Technology, 1-1-1,*

538 *Umezono, Tsukuba, Ibaraki, 305-8560, Japan.*

539 S.Y

540 *The University of Tokyo, 1-1-1, Yayoi, Bunkyo, 113-0032, Japan.*

541 M.K

542

543 **References**

- 544 Ammon CJ (1991) The isolation of receiver effects from teleseismic P waveforms.
545 *Bulletin of the Seismological Society of America* 81:2504–2510.
- 546 Araki E, Saffer DM, Kopf AJ, et al (2017) Recurring and triggered slow-slip events
547 near the trench at the Nankai Trough subduction megathrust. *Science* 356:1157–
548 1160. doi: 10.1126/science.aan3120
- 549 Bartlett WL, Friedman M, Logan JM (1981) Experimental folding and faulting of rocks
550 under confining pressure. *Tectonophysics* 79:255–277.
- 551 Brenguier F, Shapiro NM, Campillo M, et al (2007) 3-D surface wave tomography of
552 the Piton de la Fournaise volcano using seismic noise correlations. *Geophys Res*
553 *Lett* 34:1351–5. doi: 10.1029/2006GL028586
- 554 Brocher TM (2005) Empirical Relations between Elastic Wavespeeds and Density in
555 the Earth's Crust. *Bulletin of the Seismological Society of America* 95:2081–2092.

556 doi: 10.1785/0120050077

557 Clayton R, Engquist B (1977) Absorbing boundary condition for acoustic and elastic
558 wave equations. *Bulletin of the Seismological Society of America* 67:1529–1540.

559 Cochran ES, Vidale JE, Tanaka S (2004) Earth Tides Can Trigger Shallow Thrust Fault
560 Earthquakes. *Science* 306:1164–1166. doi: 10.1126/science.1103961

561 DeMets C, Gordon RG, Argus DF (2010) Geologically current plate motions.
562 *Geophysical Journal International* 181:1–80. doi: 10.1111/j.1365-
563 246X.2009.04491.x

564 Hawthorne JC, Rubin AM (2010) Tidal modulation of slow slip in Cascadia. *J Geophys*
565 *Res* 115:B09406. doi: 10.1029/2010JB007502

566 Houston H (2015) Low friction and fault weakening revealed by rising sensitivity of
567 tremor to tidal stress. *Nature Geoscience* 8:409–415. doi: 10.1038/ngeo2419

568 Ide S (2010) Striations, duration, migration and tidal response in deep tremor. *Nature*
569 466:356–360. doi: 10.1038/nature09251

570 Ide S, Yabe S, Tanaka Y (2016) Earthquake potential revealed by tidal influence on
571 earthquake size–frequency statistics. *Nature Geoscience* 9:834–837. doi:
572 10.1038/ngeo2796

573 Kimura G, Yamaguchi A, Hojo M, et al (2012) Tectonic mélange as fault rock of
574 subduction plate boundary. *Tectonophysics* 568-569:25–38. doi:
575 10.1016/j.tecto.2011.08.025

576 Kopf A, Araki E, Toczko S, Expedition 332 Scientists (2011) Proceedings of the IODP.
577 Integrated Ocean Drilling Program

578 Kopf A, Saffer D, Toczko S, Expedition 365 Scientists (2016) Expedition 365
579 preliminary report: NanTroSEIZE stage 3: Shallow megasplay Long-Term
580 Borehole Monitoring System (LTBMS) (International Ocean Discovery Program).
581 International Ocean Discovery Program

- 582 Kubo H, Nakamura T, Suzuki W, et al (2018) Site Amplification Characteristics at
583 Nankai Seafloor Observation Network, DONET1, Japan, Evaluated Using Spectral
584 Inversion. *Bulletin of the Seismological Society of America* 108:1210–1218. doi:
585 10.1785/0120170254
- 586 Lambert A, Kao H, Rogers G, Courtier N (2009) Correlation of tremor activity with
587 tidal stress in the northern Cascadia subduction zone. *J Geophys Res* 114:B00A08.
588 doi: 10.1029/2008JB006038
- 589 Langston CA (1979) Structure under Mount Rainier, Washington, inferred from
590 teleseismic body waves. *J Geophys Res* 84:4749–4762.
- 591 Nagaya M, Oda H, Akazawa H, Ishise M (2008) Receiver Functions of Seismic Waves
592 in Layered Anisotropic Media: Application to the Estimate of Seismic Anisotropy.
593 *Bulletin of the Seismological Society of America* 98:2990–3006. doi:
594 10.1785/0120080130
- 595 Nakamura M, Kakazu K (2017) Tidal sensitivity of shallow very low frequency
596 earthquakes in the Ryukyu Trench. *J Geophys Res Solid Earth* 122:1221–1238. doi:
597 10.1002/2016JB013348
- 598 Nakanishi A, Kodaira S, Miura S, et al (2008) Detailed structural image around splay-
599 fault branching in the Nankai subduction seismogenic zone: Results from a high-
600 density ocean bottom seismic survey. *J Geophys Res* 113:119–14. doi:
601 10.1029/2007JB004974
- 602 Nakata R, Suda N, Tsuruoka H (2008) Non-volcanic tremor resulting from the
603 combined effect of Earth tides and slow slip events. *Nature Geoscience* 1:676–678.
604 doi: 10.1038/ngeo288
- 605 Nishizawa O (1982) Seismic velocity anisotropy in a medium containing oriented
606 cracks -Transversely isotropic case. *Journal of Physics of the Earth* 30:331–347.
- 607 Park JO, Tsuru T, Kodaira S, et al (2002) Splay Fault Branching Along the Nankai
608 Subduction Zone. *Science* 297:1157–1160. doi: 10.1126/science.1074111

- 609 Rowe CD, Moore JC, Remitti F, the IODP Expedition 343/343T Scientists (2013) The
610 thickness of subduction plate boundary faults from the seafloor into the
611 seismogenic zone. *Geology* 41:991–994. doi: 10.1130/G34556.1
- 612 Rubinstein JL, Rocca ML, Vidale JE, et al (2008) Tidal modulation of nonvolcanic
613 tremor. *Science* 319:186–189. doi: 10.1126/science.1150558
- 614 Saenger EH, Gold N, Shapiro SA (2000) Modeling the propagation of elastic waves
615 using a modified finite-difference grid. *Wave Motion* 31:77–92.
- 616 Shapiro NM (2005) High-Resolution Surface-Wave Tomography from Ambient
617 Seismic Noise. *Science* 307:1615–1618. doi: 10.1126/science.1108339
- 618 Shiraishi K, Moore GF, Yamada Y, et al (2019) Seismogenic Zone Structures Revealed
619 by Improved 3-D Seismic Images in the Nankai Trough off Kumano. *Geochem*
620 *Geophys Geosyst* 356:1157–20. doi: 10.1029/2018GC008173
- 621 Tanaka S, Sato H, Matsumura S, Ohtake M (2006) Tidal triggering of earthquakes in
622 the subducting Philippine Sea plate beneath the locked zone of the plate interface in
623 the Tokai region, Japan. *Tectonophysics* 417:69–80. doi:
624 10.1016/j.tecto.2005.09.013
- 625 Tchalenko JS, Ambraseys NN (1970) Structural analysis of the Dasht-e Bayaz (Iran)
626 earthquake fractures. *Geological Society of America Bulletin* 81:41–60.
- 627 Tonegawa T, Fukao Y, Nishida K, et al (2013) A temporal change of shear wave
628 anisotropy within the marine sedimentary layer associated with the 2011 Tohoku-
629 Oki earthquake. *J Geophys Res Solid Earth* 118:607–615. doi: 10.1002/jgrb.50074
- 630 Tsuji T, Kamei R, Pratt RG (2014) Pore pressure distribution of a mega-splay fault
631 system in the Nankai Trough subduction zone: Insight into up-dip extent of the
632 seismogenic zone. *Earth and Planetary Science Letters* 396:165–178. doi:
633 10.1016/j.epsl.2014.04.011
- 634 Tsuji T, Tokuyama H, Costa Pisani P, Moore G (2008) Effective stress and pore
635 pressure in the Nankai accretionary prism off the Muroto Peninsula, southwestern

- 636 Japan. J Geophys Res 113:320–19. doi: 10.1029/2007JB005002
- 637 Yabe S, Tanaka Y, Houston H, Ide S (2015) Tidal sensitivity of tectonic tremors in
638 Nankai and Cascadia subduction zones. J Geophys Res Solid Earth 120:7587–7605.
639 doi: 10.1002/(ISSN)2169-9356
- 640 Yabe S, Tonegawa T, Nakano M (2019) Scaled Energy Estimation for Shallow Slow
641 Earthquakes. J Geophys Res Solid Earth 124:1507–1519. doi:
642 10.1029/2018JB016815
- 643 Yokota Y, Ishikawa T (2020) Shallow slow slip events along the Nankai Trough
644 detected by GNSS-A. Science Advances 6:eaay5786.

645

646 **Figure legends**

647 **Fig. 1 Geometry of the *Chikyu*, drilling site, and OBSs. a** Location of the drilling site
648 (C0002) and reflection profiles (Shiraishi et al. 2019) (yellow lines). **b** The red triangles
649 show the locations of the 6 OBSs. The red lines show the locations of the migration
650 images shown in Figs. 7 and 8. The yellow lines correspond to the reflection profiles
651 used in Figs. 7 and 8 (Shiraishi et al. 2019). **c** Vertical cross-section showing the
652 *Chikyu*, the *Kaimei*, the OBSs and the fault at depth. Solid and dashed lines indicate *P*
653 and *S* waves, respectively.

654

655 **Fig. 2 Ambient noise field during the drilling project. a** Geometry of D/V *Chikyu*,

656 OBS04, and borehole sensor. **b** Rotation per minute (RPM) of drill-bit during the
657 drilling project. The vertical axis is time over a 1-day period. **c** The blue, black, and red
658 dots represent the locations of the front, center, and back parts of the *Chikyu* during the
659 Julian days 1–58 in 2019. **d** Waveforms of (from top to bottom) ZZ-CCF (cross
660 correlation function) for RPM=0, TT-CCF for RPM=0, ZZ-CCF for RPM=32, and TT-
661 CCF for RPM=32. The reference site of the CCFs is OBS04, and indicates that peaks at
662 positive/negative lag time are downgoing/upgoing waves.

663

664 **Fig. 3 Airgun shot experiment from R/V Kaimei.** **a** Map showing the locations of
665 inline airgun shots from R/V *Kaimei* (black dots). All other symbols are as in Fig. 1. **b**
666 Three-component shot records observed at OBS02 at frequency bands 5–15 Hz. Left
667 and right sides of the panels represent the NNW and SSE directions.

668

669 **Fig. 4 Radial- and transverse-deconvolved waveforms (RDWs and TDWs) for D/V**
670 **Chikyu airgun and ship noise.** **a** RDWs for D/V *Chikyu* airgun (left) with 20 shots and
671 ship noise (right) during Julian days 1–58 at OBS03. The days without data (gray

672 shaded areas) correspond to the drilling period, and quiet data after day 59 correspond
673 to the period when D/V *Chikyu* moved to other sites. Arrows represent coherent signals
674 that can be observed in both the RDWs. **b** Same as panel **a**, but for TDWs. **c** (top)
675 Waveforms stacked over (black) 20 shots and (red) 58 days in panel **a**. (bottom) Cross-
676 correlation coefficients between the red and black waveforms in the top panel, with a
677 time window of 0.1 s and a time shift of 0.05 s. **d** Same as **c**, but for panel **b**. **e** Same as
678 panel **a**, but for OBS02. **f** Same as panel **a**, but for OBS05.

679

680 **Fig. 5 Transverse-deconvolved waveforms (TDWs) at each OBS.** (a–e) Same as
681 Figures 4**b** and CC in 4**d**, but for **a** OBS01, **b** OBS02, **c** OBS04, **d** OBS05, and **e**
682 OBS06.

683

684 **Fig. 6 Examples of transverse-deconvolved waveforms (TDWs) for different tidal**
685 **stress.** **a** The red and black lines represent the TDWs at high and low tide, respectively,
686 for 3 OBSs. The standard deviations are represented by pink and gray lines at high and
687 low tides, respectively, for OBS03. **b** The black line shows the differential amplitude of

688 the envelope TDWs stacked over 10–50 days in 2019 between high tide and low tide at
689 OBS03. The red line shows the amplified amplitudes of the black line, derived by using
690 eq. (4).

691

692 **Fig. 7 Tidal response of TDWs. a** Normal stress on the megasplay fault, calculated
693 from the method (Yabe et al. 2015). Normal stress values within the light-blue rectangle
694 were used to calculate the stacked envelope function in Fig. 6. Red lines represent the
695 thresholds at high and low tides. **b** Number of stacked 1-hour TDWs within 5-day
696 moving averages at (black line) high tide, (blue line) middle tide, and (red line) low
697 tide. **c** The first two panels on the left represent 5-day stacked TDWs during Julian days
698 1–60 in 2019 for high and low tides at OBS03. The frequency band is 9–15 Hz. The
699 right panel displays the time shift of each segment between high and low tides, and the
700 time window of the segment and increment are 0.2 and 0.1 s, respectively. **d** Same as
701 panel **c**, but for OBS04.

702

703 **Fig. 8 Migration images of AD-Ps projected onto the reflection images. a** Migration

704 image of amplified differential P_s amplitudes between high and low tide (eq. (4)) in the
705 TDWs projected onto the reflection image along B–B' (Fig. 1) (Shiraishi et al. 2019). **b**
706 Zoom in on the box in panel **a**. The red arrows indicate multiple weak interfaces,
707 including the megasplay fault.

708

709 **Fig. 9 Numerical simulations for P_s reflected waves.** **a** The source location of D/V
710 *Chikyu* was set at the sea surface. Bathymetry is flat. The red triangles represent the 6
711 OBSs, whose relative horizontal locations with respect to D/V *Chikyu* were preserved.
712 The physical properties at each layer are summarized in Tables 3–5. **b** P_s amplitudes
713 reflected at layer 3 as a function of V_s reductions in Table 3 for the 6 OBSs, yellow:
714 OBS01, black: OBS02, light-blue: OBS03, orange: OBS04, red: OBS05, and magenta:
715 OBS06. The two dashed arrows show the V_s reduction at OBS04 for an amplitude
716 variation of 0.0002.

717

718 **Fig. 10 Numerical simulation for the P_s amplitude reflected at the megasplay fault**
719 **containing different aspect ratios of cracks.** **a** The absolute amplitudes of P_s

720 reflection in the synthetic TDWs for the 6 OBSs, yellow: OBS01, black: OBS02, light-
721 blue: OBS03, orange: OBS04, red: OBS05, and magenta: OBS06. The inset displays the
722 synthetic TDW waveforms at OBS04, where large amplitudes were obtained at low
723 aspect ratio. **b** Sketches and circled insets show connected/less-connected fractures and
724 their associated crack geometry at high tide/low tide (macroscopic view), respectively.
725 Arrows of “fluid in” and “fluid out” indicate fluid migration from R shears.

726

727 **Fig. 11 Numerical simulation results for P_s reflected waves in anisotropic media. a**

728 Velocity model (1) with a velocity gradient above the megasplay fault at $x_2 = 4$ km. Star
729 indicates the source location. Solid and dashed lines in right panel represent 1D velocity
730 model at $(x_1, x_2) = (4.0, 4.0)$ and the original model, respectively. **b** Velocity model (2)
731 with two layers of velocity reductions and a velocity gradient above the megasplay
732 fault. **c** P_s amplitudes at OBS02 for (light-blue) model (1), (orange) model (2), and
733 (black) the original model (Fig. 4) at aspect ratio of cracks of 0.2, 0.6, and 1.0. **d** P_s
734 amplitudes at OBS02 for (red) porosity of 0.05 and (black) porosity of 0.07 (original
735 model; Fig. 10).

736 **Tables**

737 **Table 1: Deep earthquakes used for estimating site amplification.**

	Date	Latitude (°)	Longitude (°)	Depth (km)	Magnitude
Eq. 1	2019/03/16 11:07:11	32.5795	136.9545	458.0	3.2
Eq. 2	2019/03/16 20:16:16	33.0767	138.3772	365.0	3.3
Eq. 3	2019/03/20 04:17:30	34.1690	136.6558	359.9	3.0
Eq. 4	2019/03/22 17:00:18	33.6270	137.2815	368.0	3.3

738

739 **Table 2: Estimated site amplifications at each OBSs.**

	Amplification of the vertical component	Error for the vertical amplification	Amplification of the horizontal component	Error for the horizontal amplification
OBS01	1.296	0.136	14.944	1.247
OBS02	1.343	0.157	18.698	0.881
OBS03	1.476	0.118	19.446	0.777
OBS04	1.406	0.157	19.595	1.170
OBS05	1.126	0.180	14.791	1.189
OBS06	1.300	0.195	16.214	1.046

740

741 **Table 3: Effective elastic constants as a function of aspect ratio of cracks.**

Aspect ratio	C11	C12	C13	C33	C44	Vp fast (km s ⁻¹)	Vs fast (km s ⁻¹)
						Vp slow (km s ⁻¹)	Vs slow (km s ⁻¹)
1.0	40.310	19.225	19.201	40.310	10.389	4.14	2.10
0.8	40.817	19.454	19.088	39.197	10.309	4.17	2.12
						4.08	2.09
0.6	41.452	19.751	18.856	37.459	10.147	4.20	2.13
						3.99	2.08
0.4	42.249	20.142	18.351	34.457	9.791	4.24	2.15
						3.83	2.04
						4.32	2.17

0.2	43.865	20.671	17.074	28.433	8.734	3.48	1.93
-----	--------	--------	--------	--------	-------	------	------

742

743 **Table 4: Model space and physical parameters for numerical simulation.**

	Thickness (km)	V_p (km s ⁻¹)	V_s (km s ⁻¹)	Density (g cm ⁻³)
Layer 1	2	1.5	0	1
Layer 2	2	4.5	2.25	2.46
Layer 3	0.05	4.5	2.1375 (5 %) 2.0250 (10 %) 1.9125 (15 %) 1.8000 (20 %)	2.46
Layer 4	1.95	4.5	2.25	2.46

744

745 **Table 5: Model space and physical parameters for numerical simulation.**

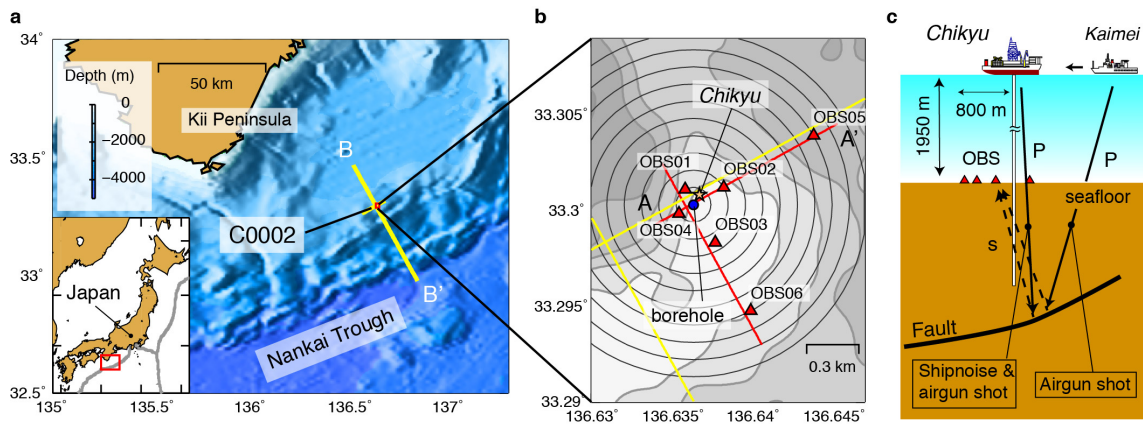
	Thickness (km)	V_p (km s ⁻¹)	V_s (km s ⁻¹)	Density (g cm ⁻³)	Dip (°)	Strike (°)
Layer 1	2	1.5	0	1		
Layer 2	2	4.5	2.25	2.46		
Layer 3	0.05	*	*	2.46	10	270
Layer 4	1.95	4.5	2.25	2.46		

746 *This value is listed in Table 4.

747

748

749 **Figures**

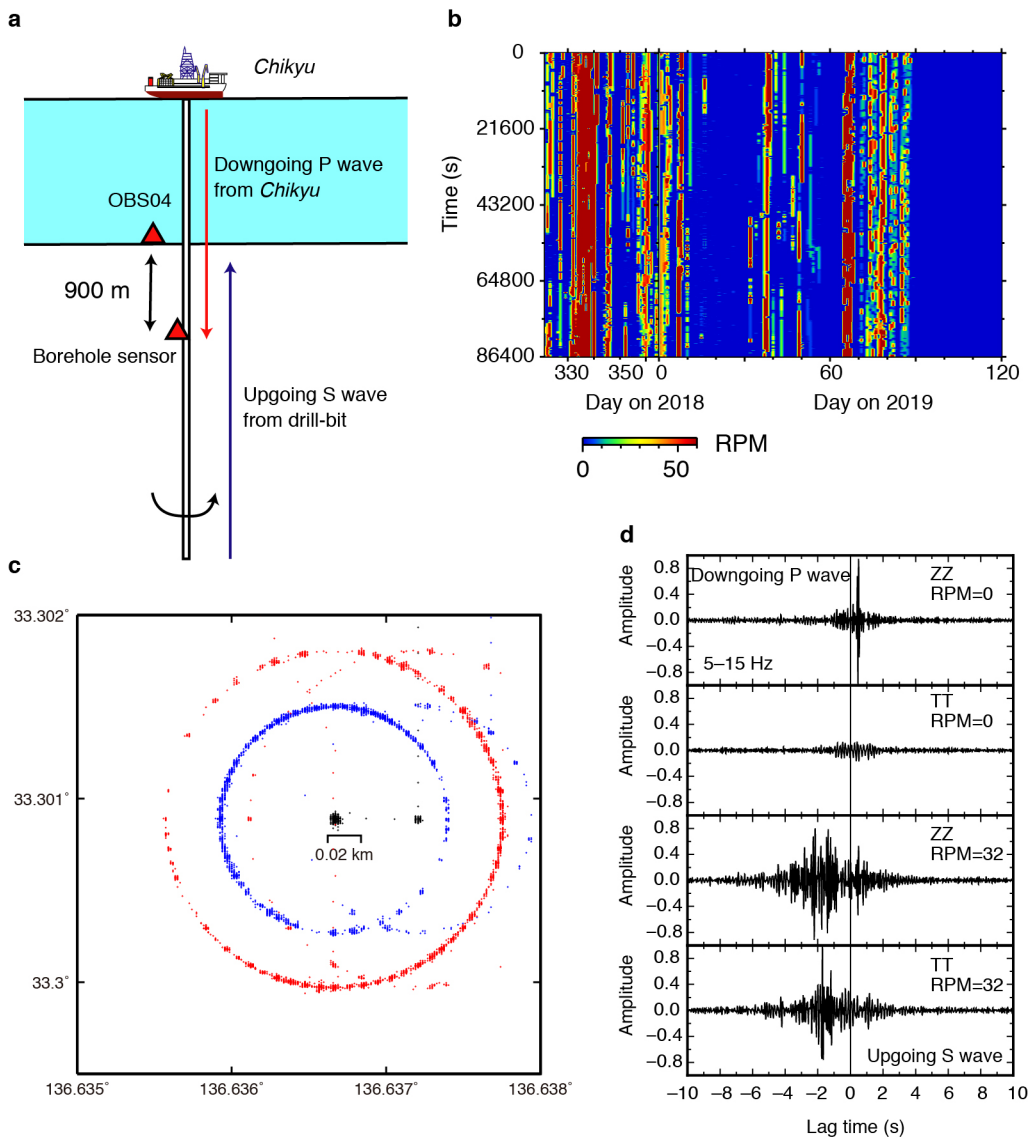


750
 751 **Fig. 1 Geometry of the *Chikyu*, drilling site, and OBSs. a** Location of the drilling site
 752 (C0002) and reflection profiles (Shiraishi et al. 2019) (yellow lines). **b** The red triangles
 753 show the locations of the 6 OBSs. The red lines show the locations of the migration
 754 images shown in Figs. 7 and 8. The yellow lines correspond to the reflection profiles
 755 used in Figs. 7 and 8 (Shiraishi et al. 2019). **c** Vertical cross-section showing the
 756 *Chikyu*, the *Kaimei*, the OBSs and the fault at depth. Solid and dashed lines indicate *P*
 757 and *S* waves, respectively.

758

759

Fig. 2

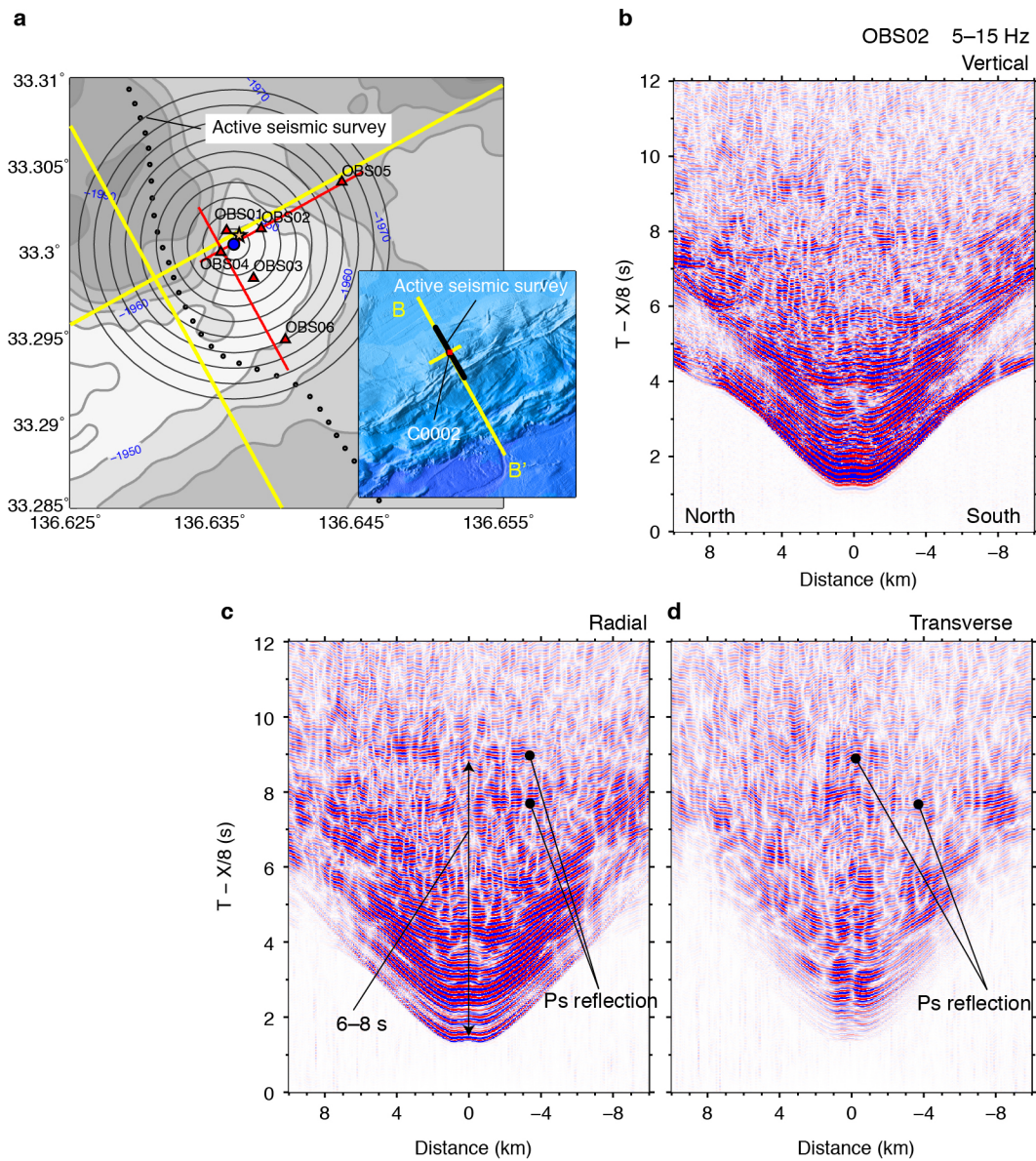


760

761 **Fig. 2 Ambient noise field during the drilling project.** **a** Geometry of D/V *Chikyu*,
 762 OBS04, and borehole sensor. **b** Rotation per minute (RPM) of drill-bit during the
 763 drilling project. The vertical axis is time over a 1-day period. **c** The blue, black, and red
 764 dots represent the locations of the front, center, and back parts of the *Chikyu* during the
 765 Julian days 1–58 in 2019. **d** Waveforms of (from top to bottom) ZZ-CCF (cross
 766 correlation function) for RPM=0, TT-CCF for RPM=0, ZZ-CCF for RPM=32, and TT-
 767 CCF for RPM=32. The reference site of the CCFs is OBS04, and indicates that peaks at
 768 positive/negative lag time are downgoing/upgoing waves.

769

Fig. 3

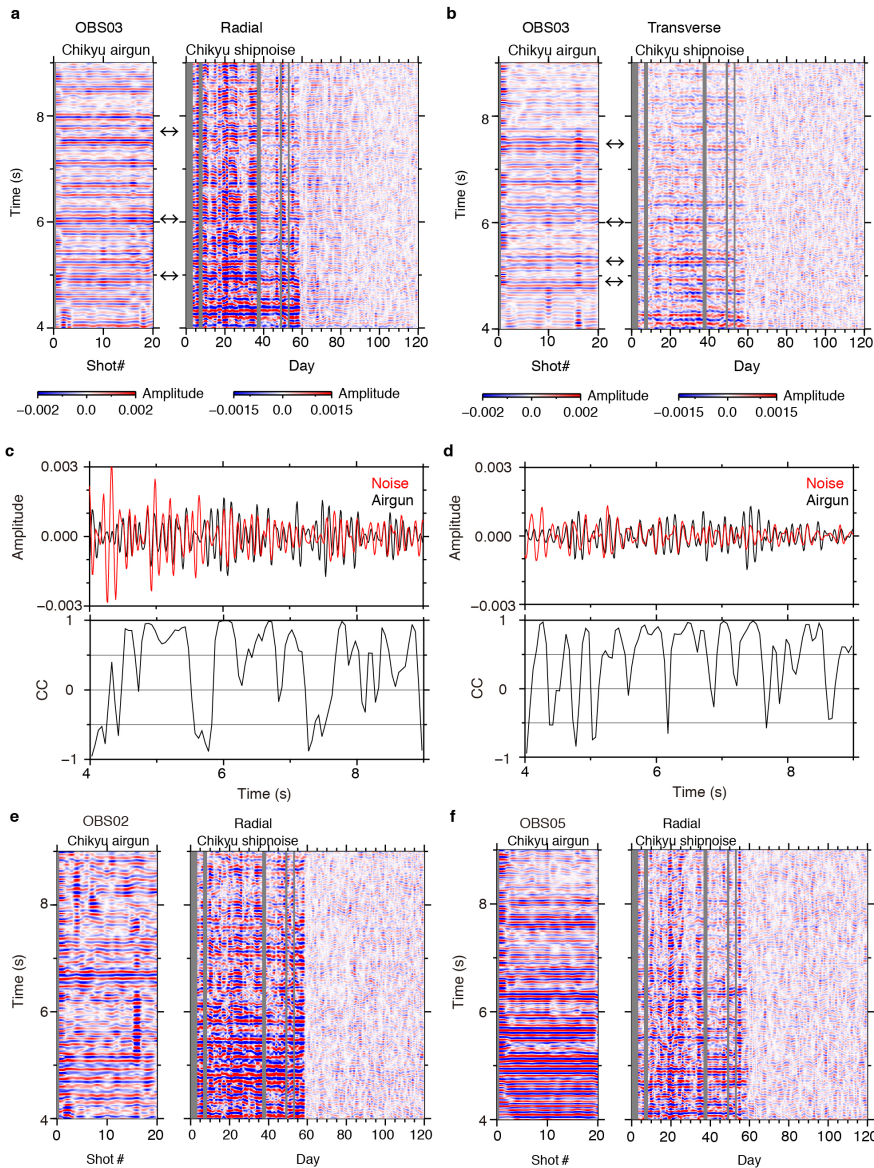


770

771 **Fig. 3** Airgun shot experiment from R/V *Kaimei*. **a** Map showing the locations of
772 inline airgun shots from R/V *Kaimei* (black dots). All other symbols are as in Fig. 1. **b**
773 Three-component shot records observed at OBS02 at frequency bands 5–15 Hz. Left
774 and right sides of the panels represent the NNW and SSE directions.

775

Fig. 4



776

777

778

779

780

781

782

783

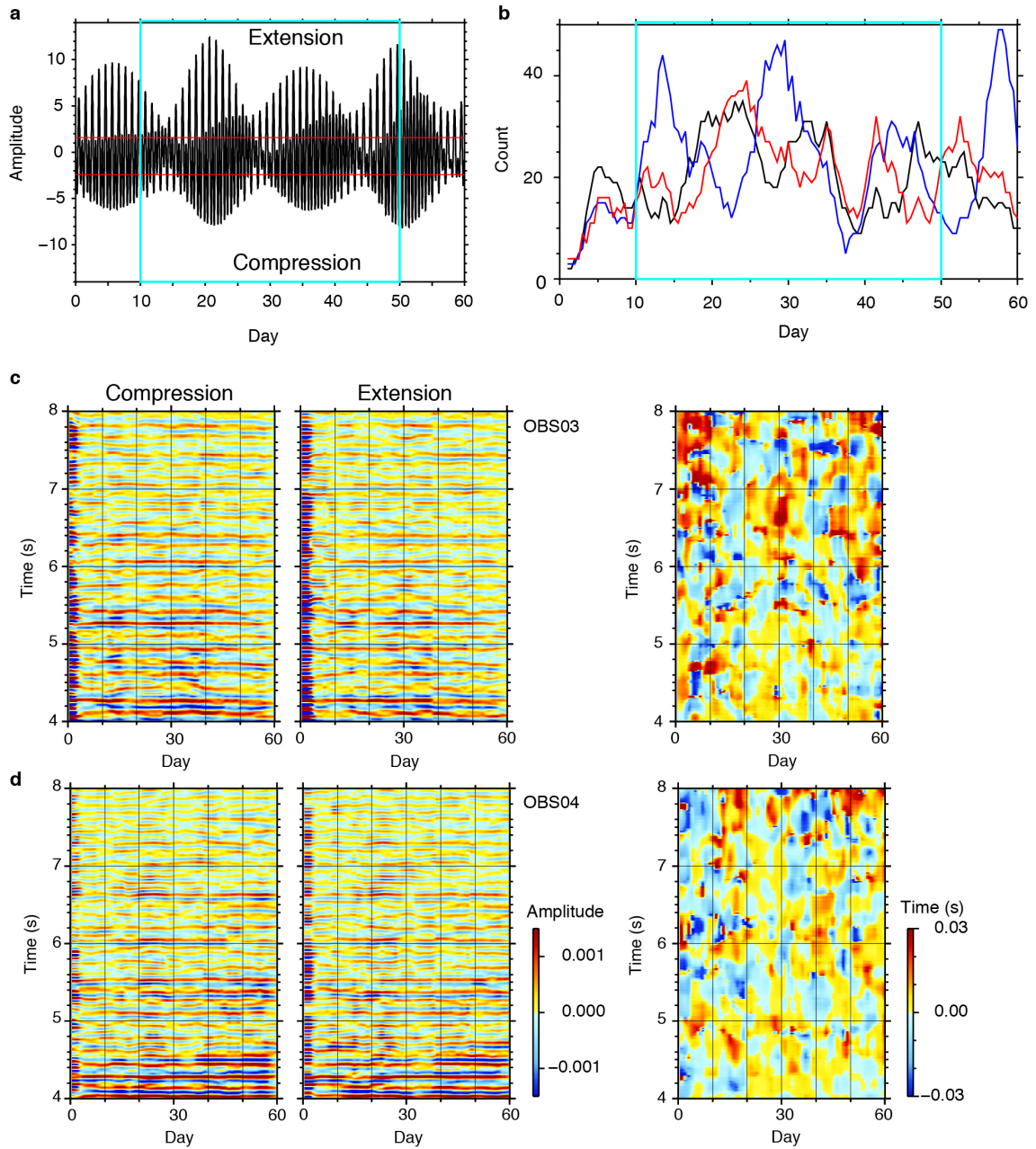
784

785

786

Fig. 4 Radial- and transverse-deconvolved waveforms (RDWs and TDWs) for D/V Chikyu airgun and ship noise. a RDWs for D/V *Chikyu* airgun (left) with 20 shots and ship noise (right) during Julian days 1–58 at OBS03. The days without data (gray shaded areas) correspond to the drilling period, and quiet data after day 59 correspond to the period when D/V *Chikyu* moved to other sites. Arrows represent coherent signals that can be observed in both the RDWs. **b** Same as panel **a**, but for TDWs. **c** (top) Waveforms stacked over (black) 20 shots and (red) 58 days in panel **a**. (bottom) Cross-correlation coefficients between the red and black waveforms in the top panel, with a time window of 0.1 s and a time shift of 0.05 s. **d** Same as **c**, but for panel **b**. **e** Same as panel **a**, but for OBS02. **f** Same as panel **a**, but for OBS05.

Fig. 5



787

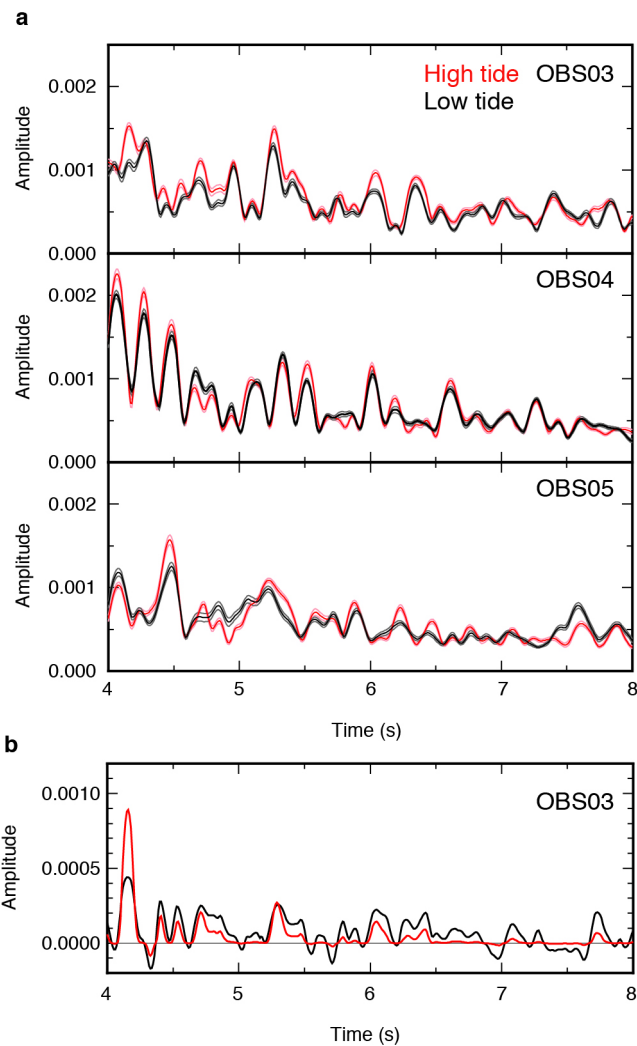
788 **Fig. 5** Transverse-deconvolved waveforms (TDWs) at each OBS. (a–e) Same as

789 Figures 4b and CC in 4d, but for a OBS01, b OBS02, c OBS04, d OBS05, and e

790 OBS06.

791

Fig. 6

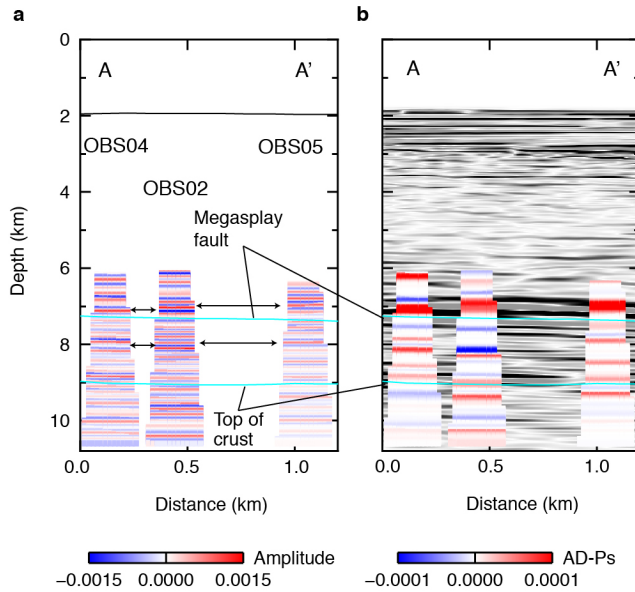


792

793 **Fig. 6** Examples of transverse-deconvolved waveforms (TDWs) for different tidal
794 **stress.** **a** The red and black lines represent the TDWs at high and low tide, respectively,
795 for 3 OBSs. The standard deviations are represented by pink and gray lines at high and
796 low tides, respectively, for OBS03. **b** The black line shows the differential amplitude of
797 the envelope TDWs stacked over 10–50 days in 2019 between high tide and low tide at
798 OBS03. The red line shows the amplified amplitudes of the black line, derived by using
799 eq. (4).

800

Fig. 7



801

802

803

804

805

806

807

808

809

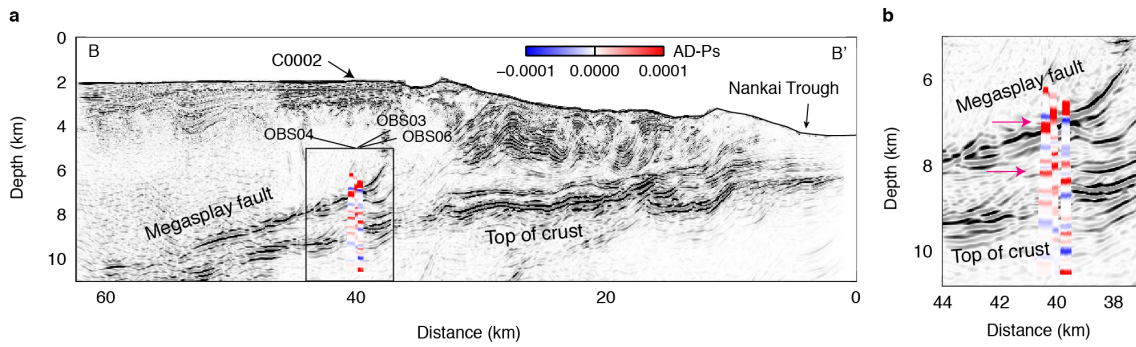
810

811

812

Fig. 7 Tidal response of TDWs. **a** Normal stress on the megasplay fault, calculated from the method (Yabe et al. 2015). Normal stress values within the light-blue rectangle were used to calculate the stacked envelope function in Fig. 6. Red lines represent the thresholds at high and low tides. **b** Number of stacked 1-hour TDWs within 5-day moving averages at (black line) high tide, (blue line) middle tide, and (red line) low tide. **c** The first two panels on the left represent 5-day stacked TDWs during Julian days 1–60 in 2019 for high and low tides at OBS03. The frequency band is 9–15 Hz. The right panel displays the time shift of each segment between high and low tides, and the time window of the segment and increment are 0.2 and 0.1 s, respectively. **d** Same as panel **c**, but for OBS04.

Fig. 8

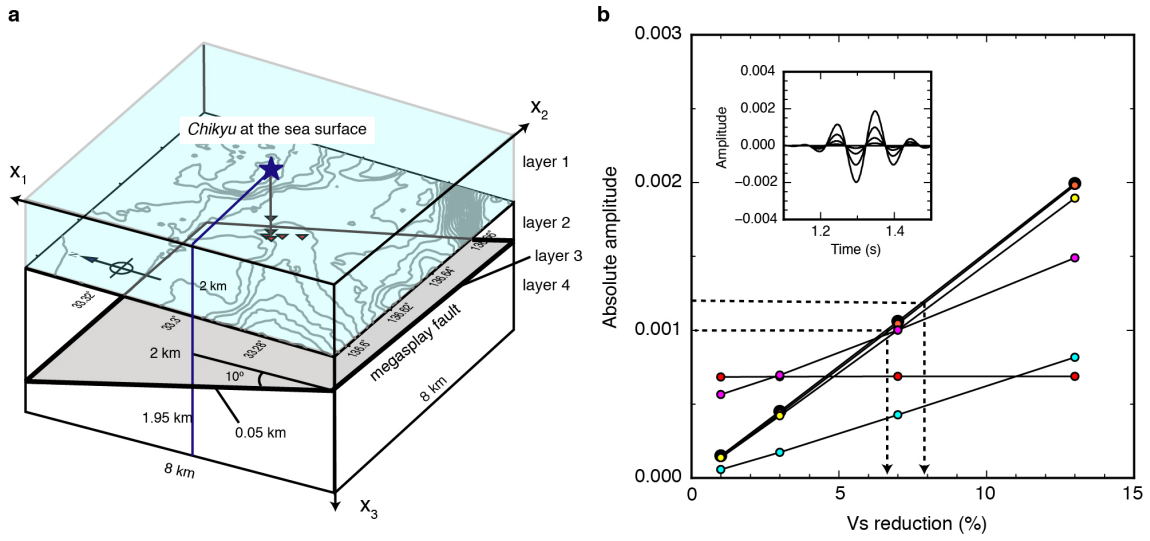


813

814 **Fig. 8 Migration images of AD-Ps projected onto the reflection images.** **a** Migration
815 image of amplified differential P s amplitudes between high and low tide (eq. (4)) in the
816 TDWs projected onto the reflection image along B–B' (Fig. 1) (Shiraishi et al. 2019). **b**
817 Zoom in on the box in panel **a**. The red arrows indicate multiple weak interfaces,
818 including the megasplay fault.

819

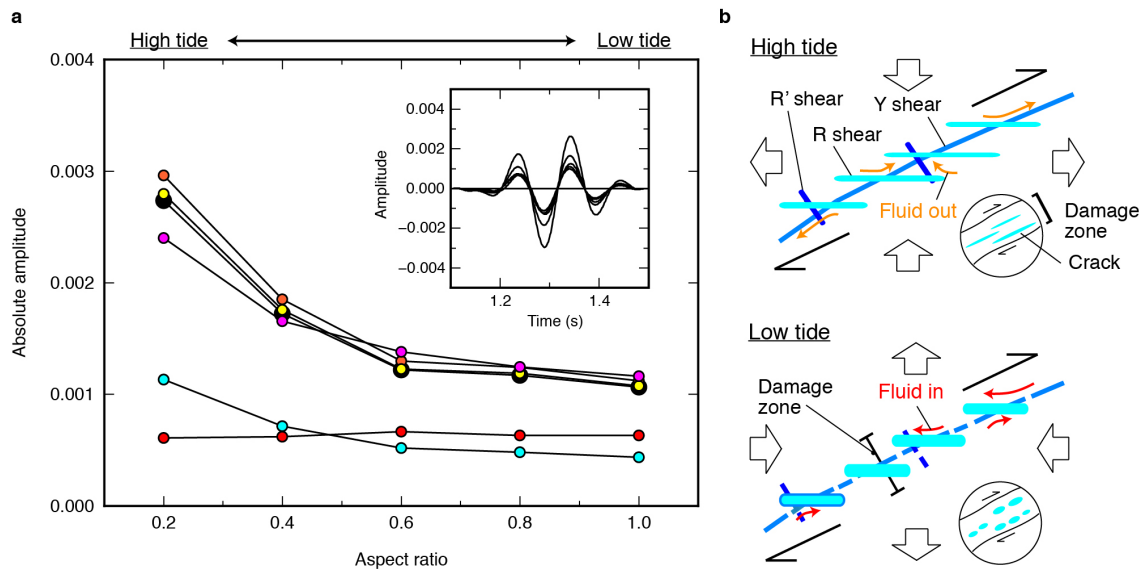
Fig. 9



820

821 **Fig. 9 Numerical simulations for Ps reflected waves.** **a** The source location of D/V
 822 *Chikyu* was set at the sea surface. Bathymetry is flat. The red triangles represent the 6
 823 OBSs, whose relative horizontal locations with respect to D/V *Chikyu* were preserved.
 824 The physical properties at each layer are summarized in Tables 3–5. **b** *Ps* amplitudes
 825 reflected at layer 3 as a function of *Vs* reductions in Table 3 for the 6 OBSs, yellow:
 826 OBS01, black: OBS02, light-blue: OBS03, orange: OBS04, red: OBS05, and magenta:
 827 OBS06. The two dashed arrows show the *Vs* reduction at OBS04 for an amplitude
 828 variation of 0.0002.

829



830

831 **Fig. 10 Numerical simulation for the P_s amplitude reflected at the megasplay fault**

832 **containing different aspect ratios of cracks. a** The absolute amplitudes of P_s

833 reflection in the synthetic TDWs for the 6 OBSs, yellow: OBS01, black: OBS02, light-

834 blue: OBS03, orange: OBS04, red: OBS05, and magenta: OBS06. The inset displays the

835 synthetic TDW waveforms at OBS04, where large amplitudes were obtained at low

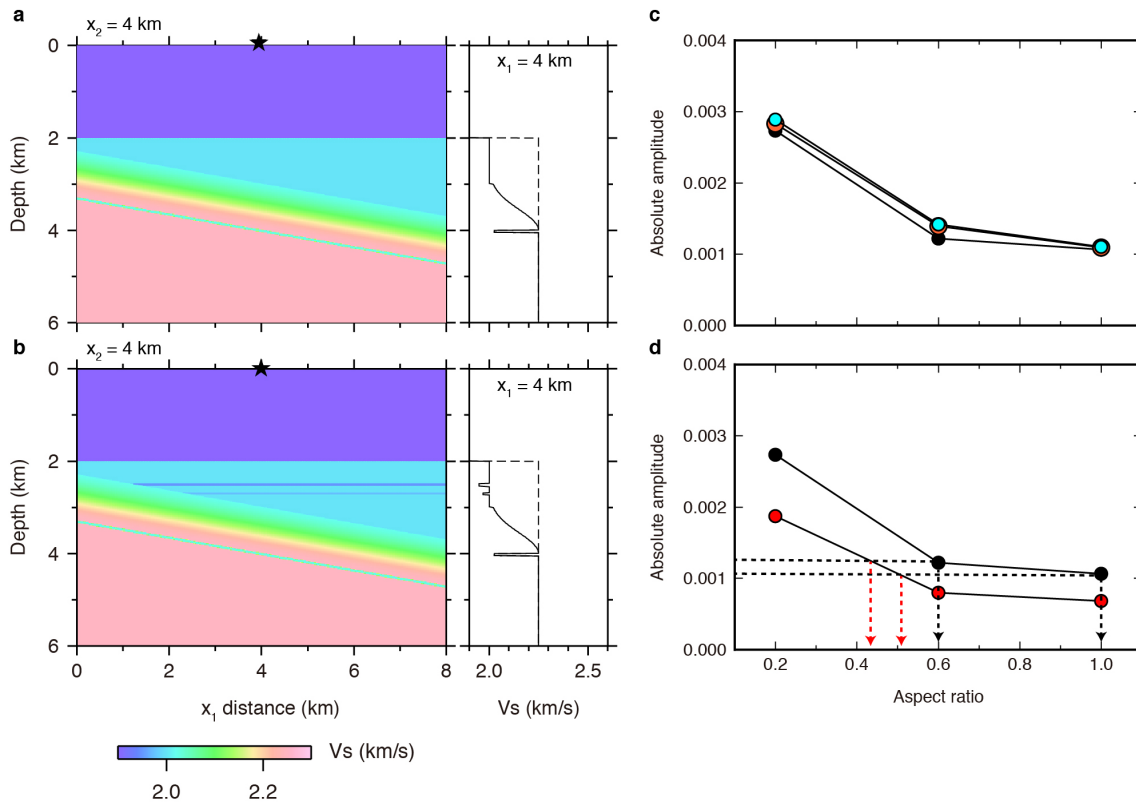
836 aspect ratio. **b** Sketches and circled insets show connected/less-connected fractures and

837 their associated crack geometry at high tide/low tide (macroscopic view), respectively.

838 Arrows of “fluid in” and “fluid out” indicate fluid migration from R shears.

839

Fig. 11



840

841 **Fig. 11 Numerical simulation results for Ps reflected waves in anisotropic media. a**

842 Velocity model (1) with a velocity gradient above the megasplay fault at $x_2 = 4$ km. Star

843 indicates the source location. Solid and dashed lines in right panel represent 1D velocity

844 model at $(x_1, x_2) = (4.0, 4.0)$ and the original model, respectively. **b** Velocity model (2)

845 with two layers of velocity reductions and a velocity gradient above the megasplay

846 fault. **c** Ps amplitudes at OBS02 for (light-blue) model (1), (orange) model (2), and

847 (black) the original model (Fig. 4) at aspect ratio of cracks of 0.2, 0.6, and 1.0. **d** Ps

848 amplitudes at OBS02 for (red) porosity of 0.05 and (black) porosity of 0.07 (original

849 model; Fig. 10).

850

851

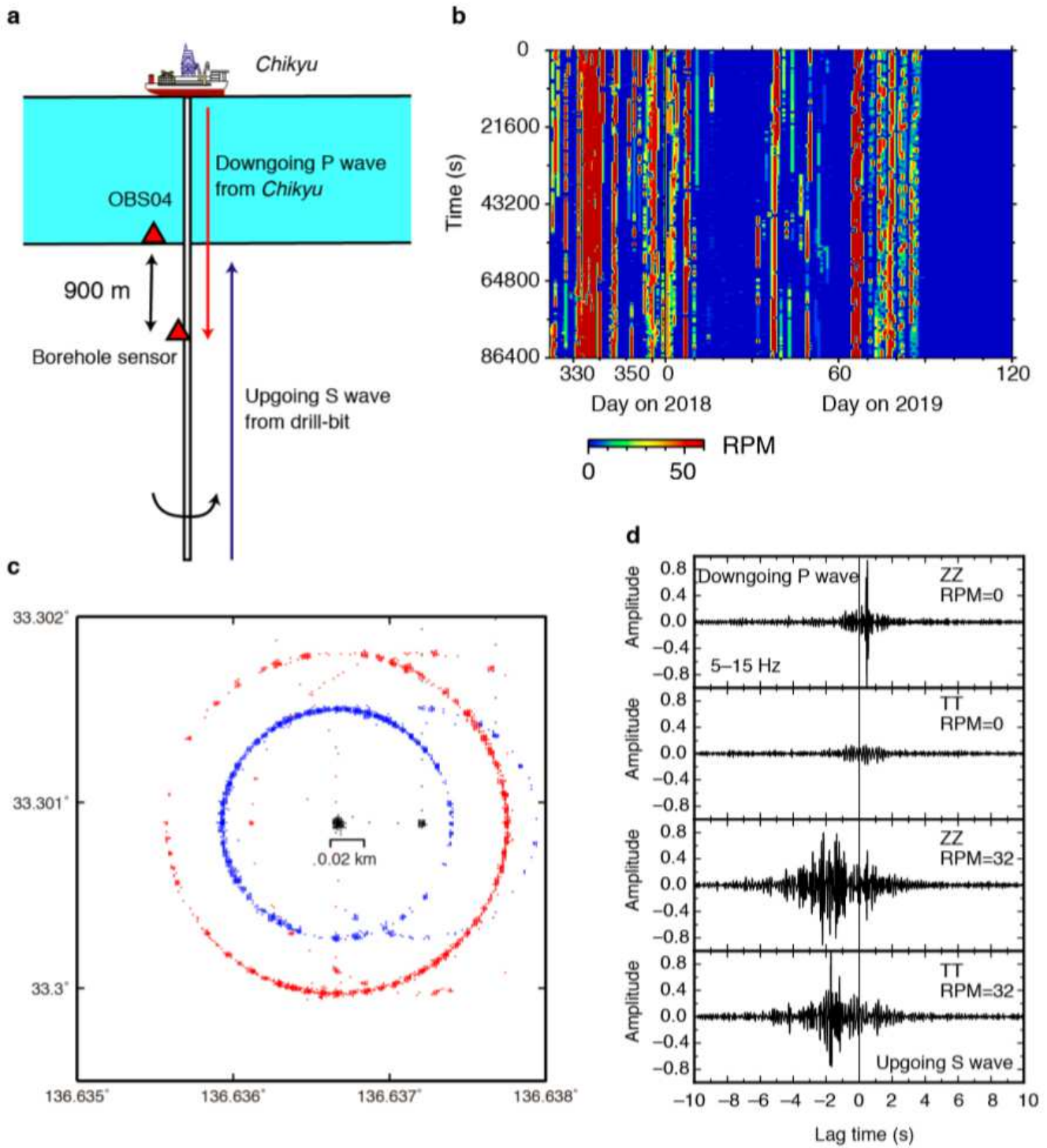


Figure 2

Ambient noise field during the drilling project. a Geometry of D/V Chikyu, OBS04, and borehole sensor. b Rotation per minute (RPM) of drill-bit during the drilling project. The vertical axis is time over a 1-day period. c The blue, black, and red dots represent the locations of the front, center, and back parts of the Chikyu during the Julian days 1–58 in 2019. d Waveforms of (from top to bottom) ZZ-CCF (cross correlation function) for RPM=0, TT-CCF for RPM=0, ZZ-CCF for RPM=32, and TT-CCF for RPM=32. The

reference site of the CCFs is OBS04, and indicates that peaks at positive/negative lag time are downgoing/upgoing waves.

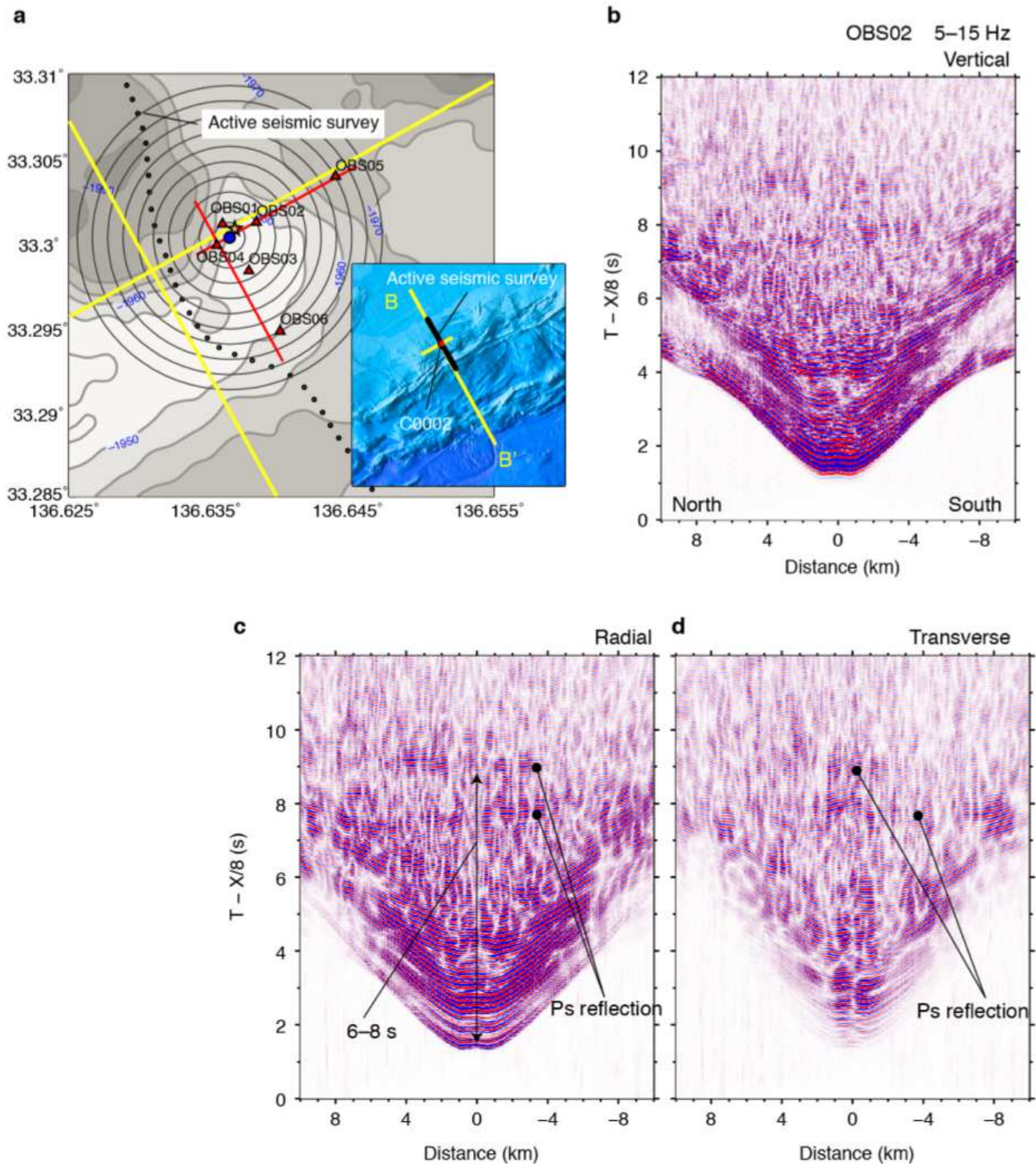


Figure 3

Airgun shot experiment from R/V Kaimei. a Map showing the locations of inline airgun shots from R/V Kaimei (black dots). All other symbols are as in Fig. 1. b Three-component shot records observed at

OBS02 at frequency bands 5–15 Hz. Left and right sides of the panels represent the NNW and SSE directions.

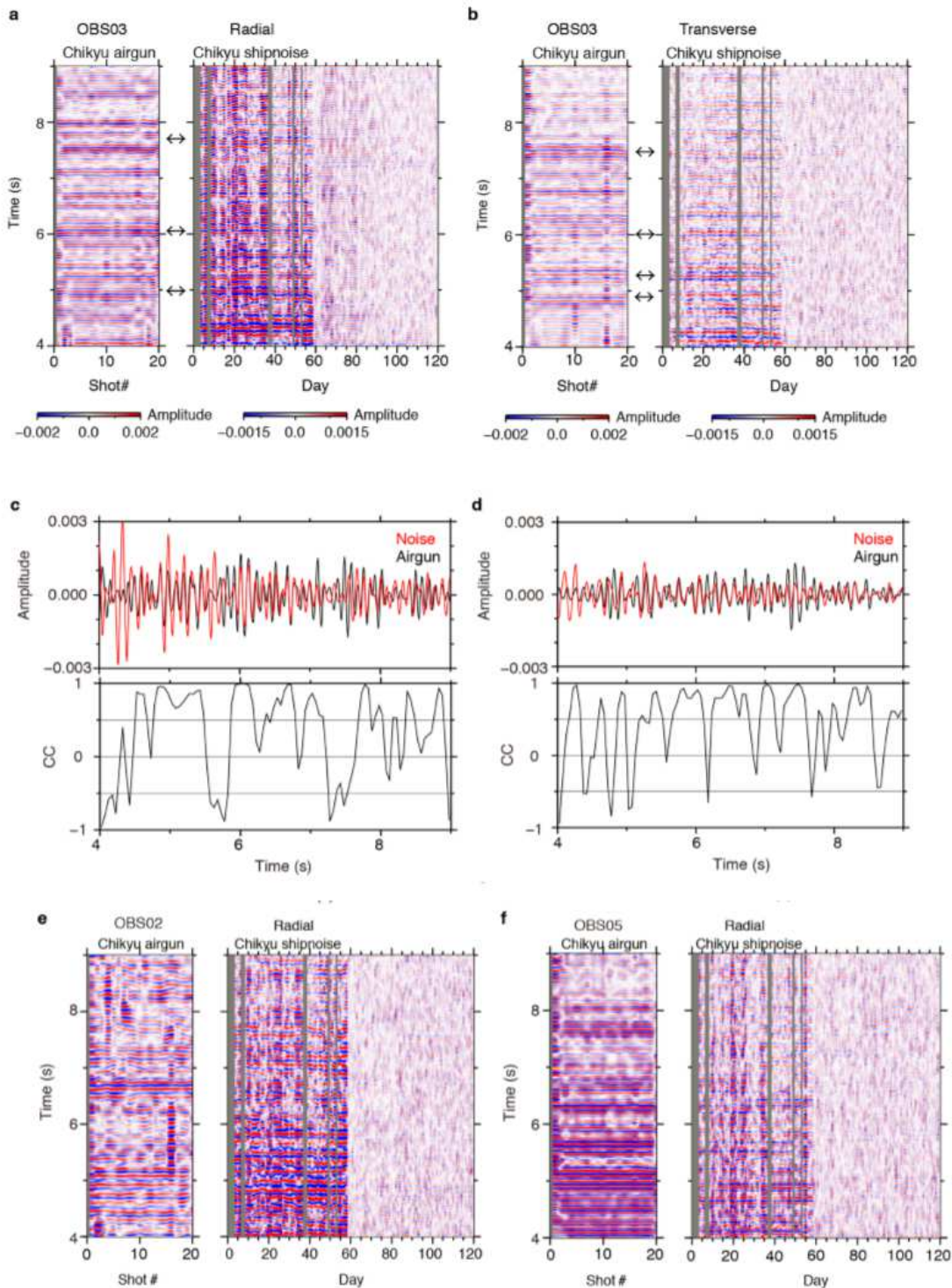


Figure 4

Radial- and transverse-deconvolved waveforms (RDWs and TDWs) for D/V Chikyu airgun and ship noise. a RDWs for D/V Chikyu airgun (left) with 20 shots and ship noise (right) during Julian days 1–58 at OBS03. The days without data (gray shaded areas) correspond to the drilling period, and quiet data after

day 59 correspond to the period when D/V Chikyu moved to other sites. Arrows represent coherent signals that can be observed in both the RDWs. b Same as panel a, but for TDWs. c (top) Waveforms stacked over (black) 20 shots and (red) 58 days in panel a. (bottom) Cross-correlation coefficients between the red and black waveforms in the top panel, with a time window of 0.1 s and a time shift of 0.05 s. d Same as c, but for panel b. e Same as panel a, but for OBS02. f Same as panel a, but for OBS05.

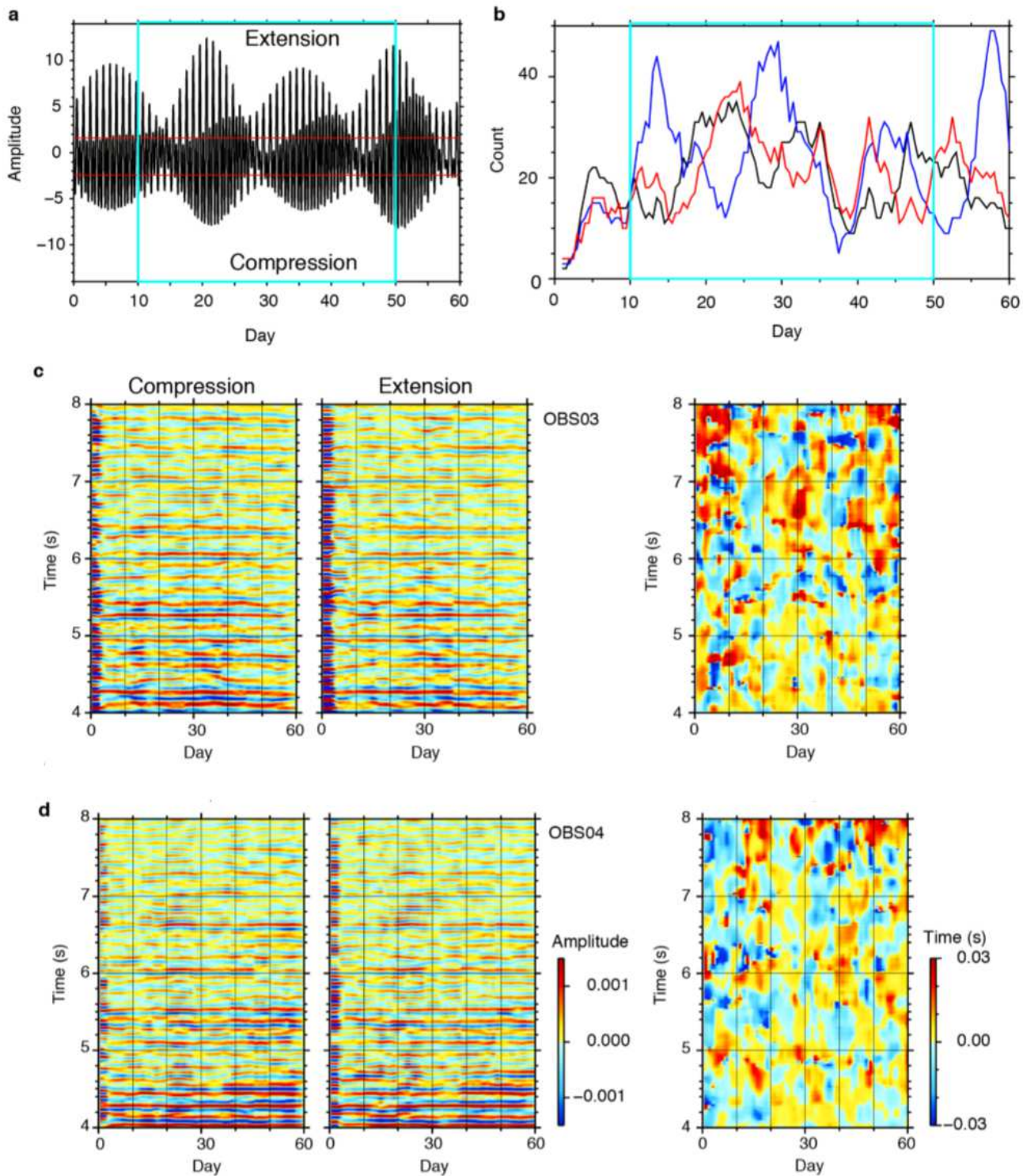


Figure 5

Transverse-deconvolved waveforms (TDWs) at each OBS. (a–e) Same as Figures 4b and CC in 4d, but for a OBS01, b OBS02, c OBS04, d OBS05, and e OBS06.

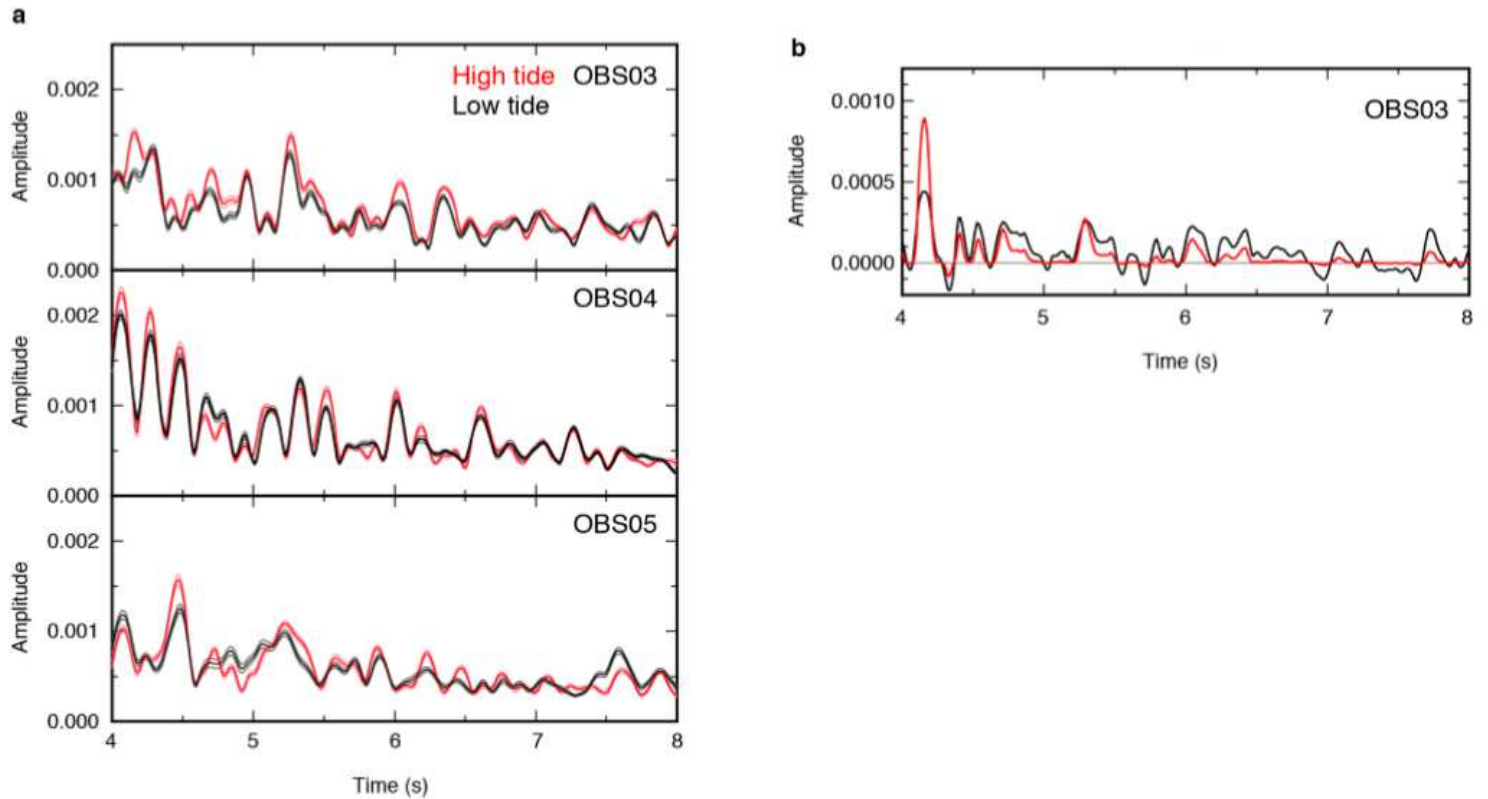


Figure 6

Examples of transverse-deconvolved waveforms (TDWs) for different tidal stress. a The red and black lines represent the TDWs at high and low tide, respectively for 3 OBSs. The standard deviations are represented by pink and gray lines at high and low tides, respectively, for OBS03. b The black line shows the differential amplitude of the envelope TDWs stacked over 10–50 days in 2019 between high tide and low tide at OBS03. The red line shows the amplified amplitudes of the black line, derived by using eq. (4).

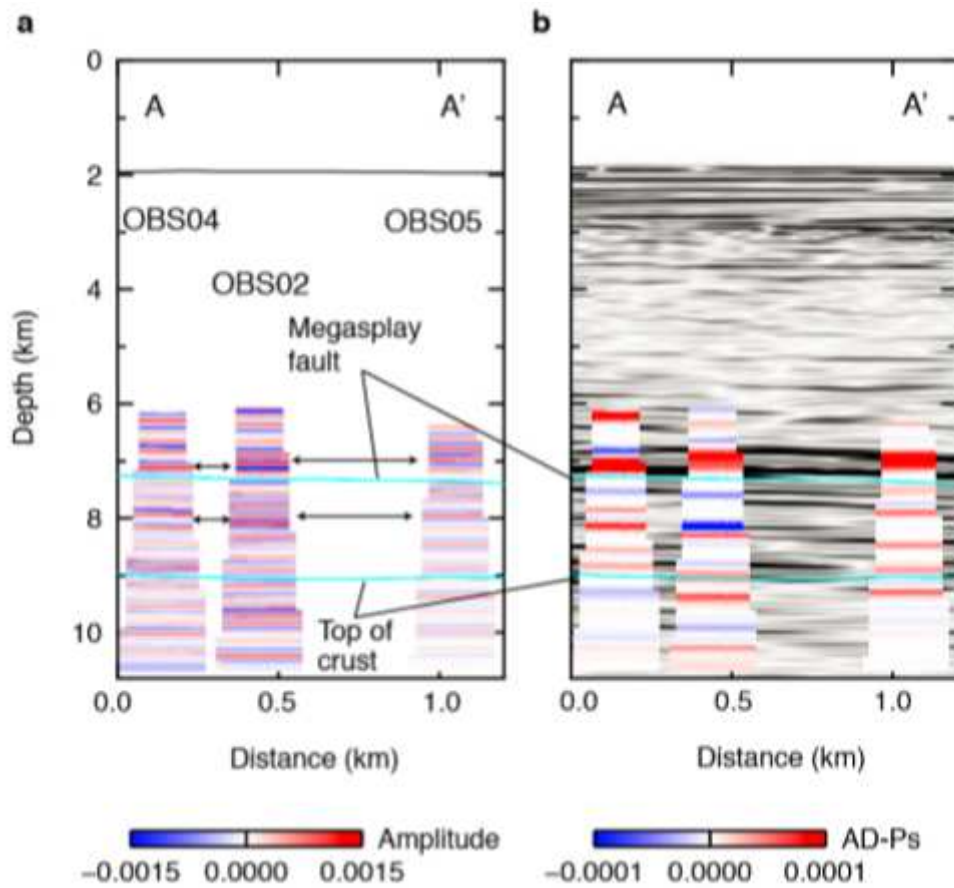


Figure 7

Tidal response of TDWs. a Normal stress on the megasplay fault, calculated from the method (Yabe et al. 2015). Normal stress values within the light-blue rectangle were used to calculate the stacked envelope function in Fig. 6. Red lines represent the thresholds at high and low tides. b Number of stacked 1-hour TDWs within 5-day moving averages at (black line) high tide, (blue line) middle tide, and (red line) low tide. c The first two panels on the left represent 5-day stacked TDWs during Julian days 1–60 in 2019 for high and low tides at OBS03. The frequency band is 9–15 Hz. The right panel displays the time shift of each segment between high and low tides, and the time window of the segment and increment are 0.2 and 0.1 s, respectively. d Same as panel c, but for OBS04.

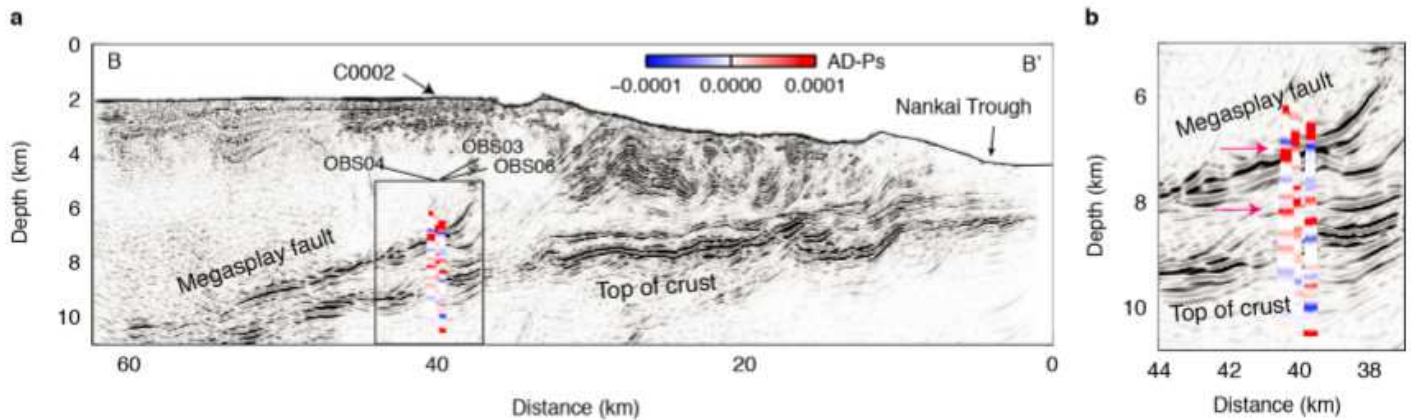


Figure 8

Migration images of AD-Ps projected onto the reflection images. a Migration image of amplified differential Ps amplitudes between high and low tide (eq. (4)) in the TDWs projected onto the reflection image along B–B' (Fig. 1) (Shiraishi et al. 2019). b Zoom in on the box in panel a. The red arrows indicate multiple weak interfaces, including the megasplay fault.

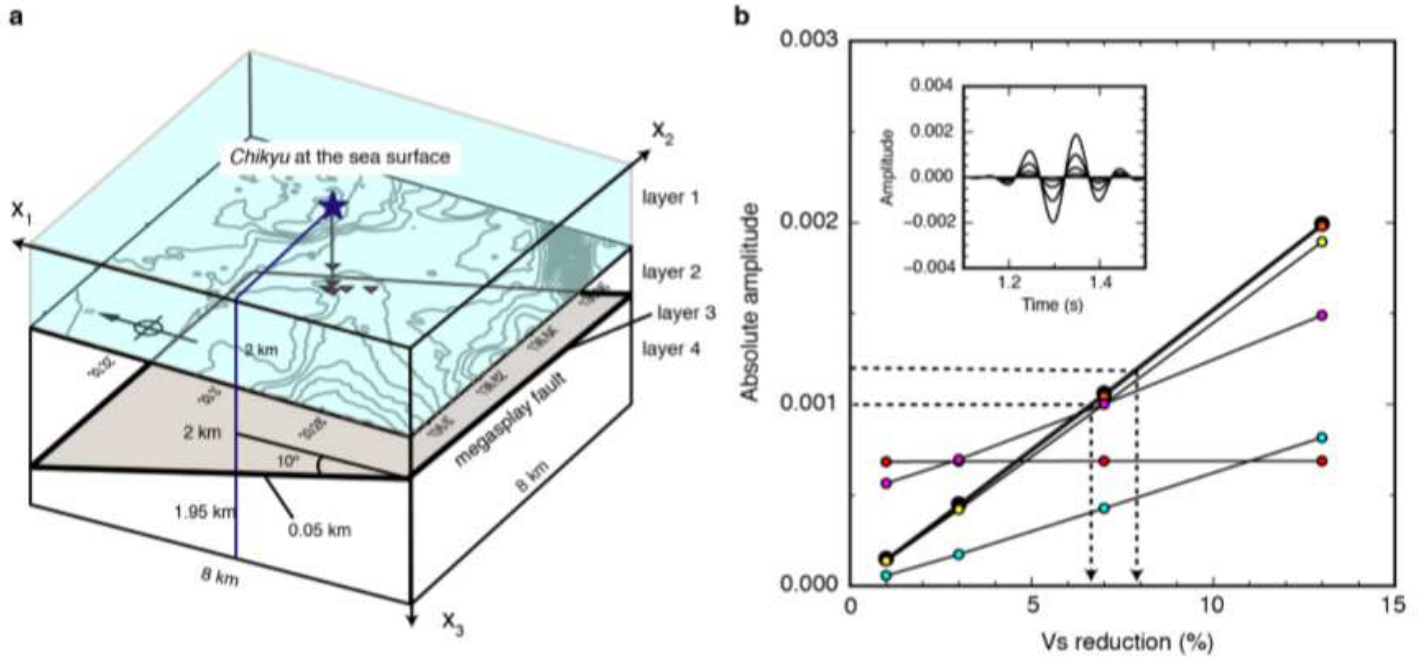


Figure 9

Numerical simulations for Ps reflected waves. a The source location of D/V Chikyu was set at the sea surface. Bathymetry is flat. The red triangles represent the 6 OBSs, whose relative horizontal locations with respect to D/V Chikyu were preserved. The physical properties at each layer are summarized in Tables 3–5. b Ps amplitudes reflected at layer 3 as a function of Vs reductions in Table 3 for the 6 OBSs, yellow: OBS01, black: OBS02, light-blue: OBS03, orange: OBS04, red: OBS05, and magenta: OBS06. The two dashed arrows show the Vs reduction at OBS04 for an amplitude variation of 0.0002.

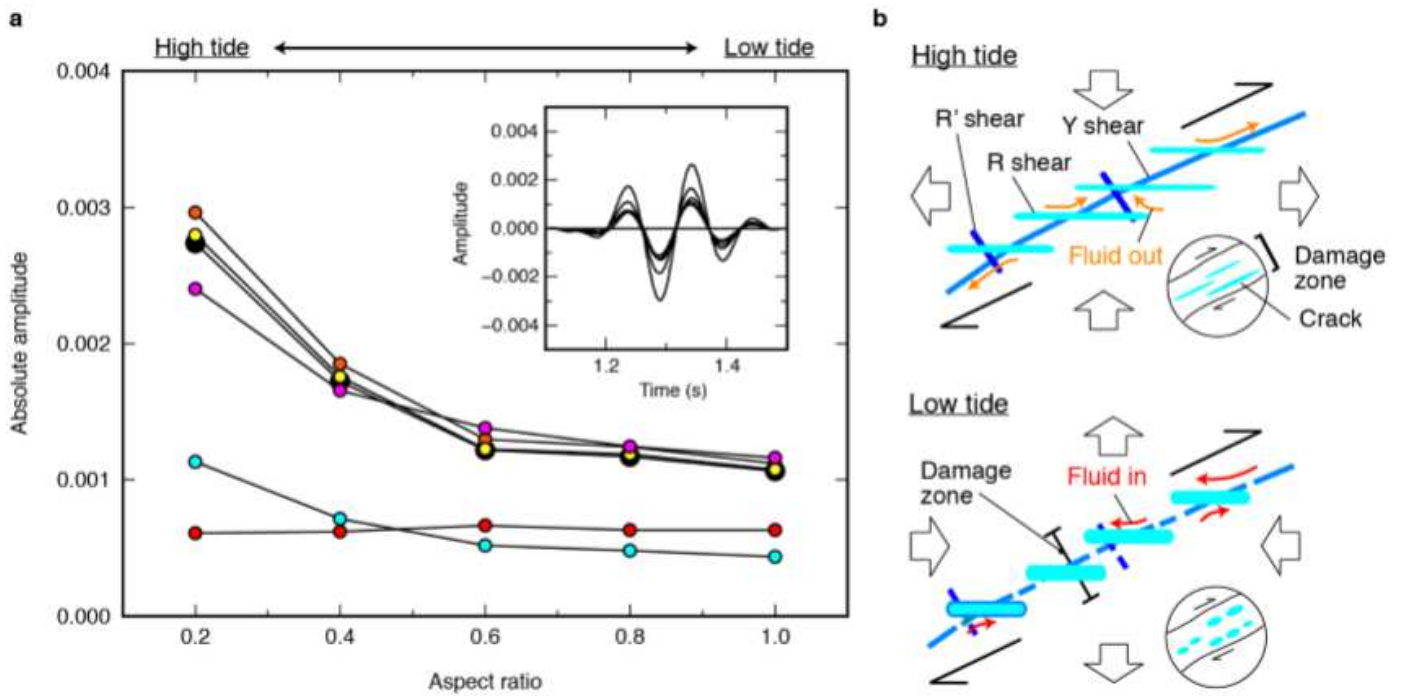


Figure 10

Numerical simulation for the Ps amplitude reflected at the megasplay fault containing different aspect ratios of cracks. a The absolute amplitudes of Ps reflection in the synthetic TDWs for the 6 OBSs, yellow: OBS01, black: OBS02, light- blue: OBS03, orange: OBS04, red: OBS05, and magenta: OBS06. The inset displays the synthetic TDW waveforms at OBS04, where large amplitudes were obtained at low aspect ratio. b Sketches and circled insets show connected/less-connected fractures and their associated crack geometry at high tide/low tide (macroscopic view), respectively. Arrows of “fluid in” and “fluid out” indicate fluid migration from R shears.

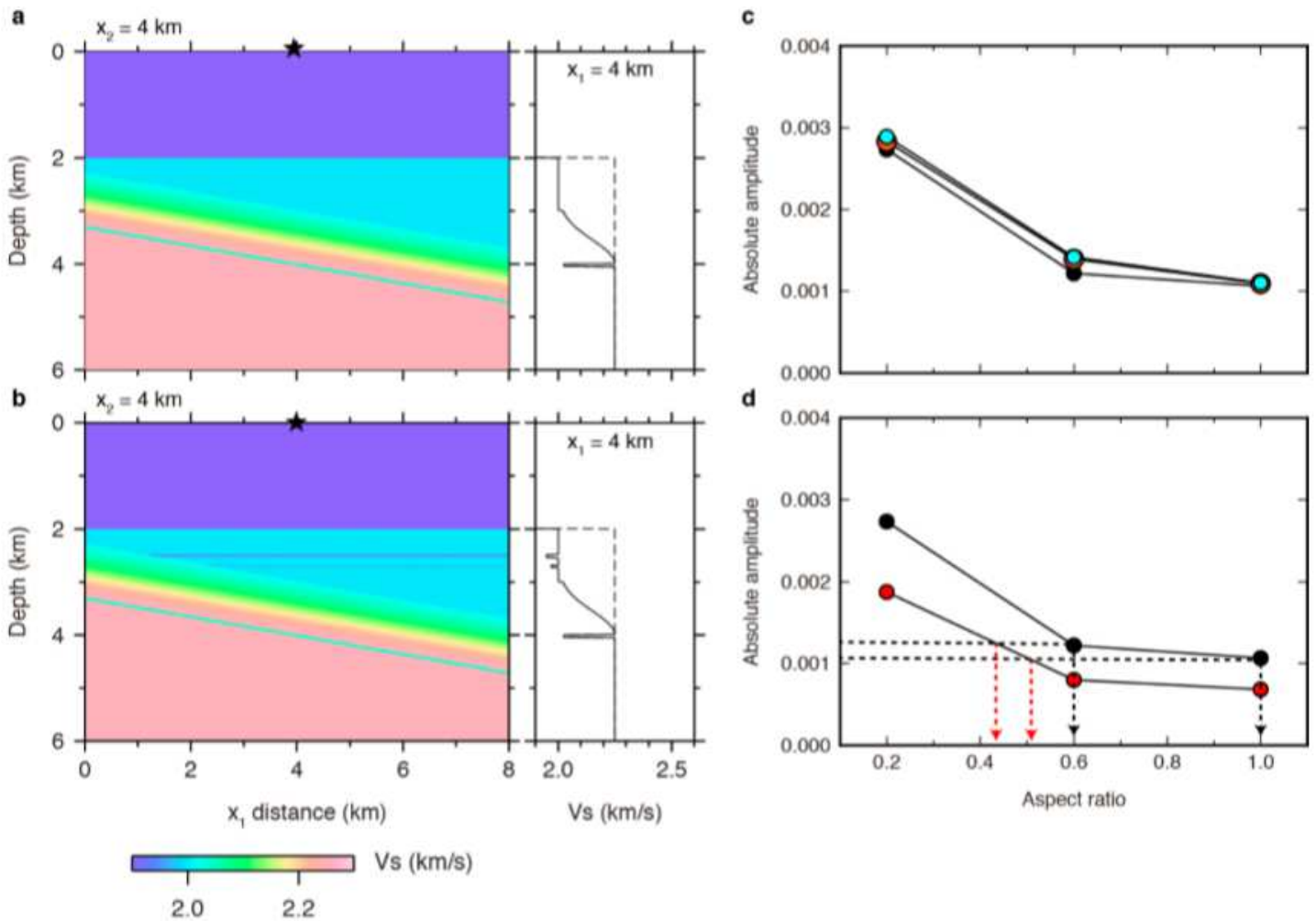


Figure 11

Numerical simulation results for Ps reflected waves in anisotropic media. a Velocity model (1) with a velocity gradient above the megasplay fault at $x_2 = 4$ km. Star indicates the source location. Solid and dashed lines in right panel represent 1D velocity model at $(x_1, x_2) = (4.0, 4.0)$ and the original model, respectively. b Velocity model (2) with two layers of velocity reductions and a velocity gradient above the megasplay fault. c Ps amplitudes at OBS02 for (light-blue) model (1), (orange) model (2), and (black) the original model (Fig. 4) at aspect ratio of cracks of 0.2, 0.6, and 1.0. d Ps amplitudes at OBS02 for (red) porosity of 0.05 and (black) porosity of 0.07 (original model; Fig. 10).

Supplementary Files

This is a list of supplementary files associated with this preprint. Click to download.

- [Supplement.pdf](#)
- [graphicalabstver2.jpg](#)